Modeling the basal melting and marine ice accretion of the Amery Ice Shelf

B. K. Galton-Fenzi,[1] J. R. Hunter,[1] R. Coleman,[2] S. J. Marsland,[3] and R. C. Warner[1,4]

Received 18 May 2012; revised 2 August 2012; accepted 13 August 2012; published 26 September 2012.

[1] The basal mass balance of the Amery Ice Shelf (AIS) in East Antarctica is investigated using a numerical ocean model. The main improvements of this model over previous studies are the inclusion of frazil formation and dynamics, tides and the use of the latest estimate of the sub-ice-shelf cavity geometry. The model produces a net basal melt rate of 45.6 Gt year^{-1} (0.74 m ice year^{-1}) which is in good agreement with reviewed observations. The melting at the base of the ice shelf is primarily due to interaction with High Salinity Shelf Water created from the surface sea-ice formation in winter. The temperature difference between the coldest waters created in the open ocean and the *in situ* freezing point of ocean water in contact with the deepest part of the AIS drives a melt rate that can exceed 30 m of ice year^{-1}. The inclusion of frazil dynamics is shown to be important for both melting and marine ice accretion (refreezing). Frazil initially forms in the supercooled water layer adjacent to the base of the ice shelf. The net accretion of marine ice is 5.3 Gt year^{-1}, comprised of 3.7 Gt year^{-1} of frazil accretion and 1.6 Gt year^{-1} of direct basal refreezing.

Citation: Galton-Fenzi, B. K., J. R. Hunter, R. Coleman, S. J. Marsland, and R. C. Warner (2012), Modeling the basal melting and marine ice accretion of the Amery Ice Shelf, *J. Geophys. Res.*, *117*, C09031, doi:10.1029/2012JC008214.

1. Introduction

[2] The Amery Ice Shelf (AIS) is the major embayed ice shelf of East Antarctica (Figure 1) with an area of ~60 000 km^2 [*Galton-Fenzi et al.*, 2008]. The AIS has some of the deepest Antarctic ice (~2500 m below sea level) in contact with the ocean [*Fricker et al.*, 2000]. About 16% of the grounded East Antarctic Ice Sheet area drains through the Lambert and other tributary glaciers [*Allison*, 1979]. Ice flux calculations of *Yu et al.* [2010] show that the Lambert-Mellor-Fisher (LMF) tributary glacial systems combine to contribute 60.5% of the total ice mass flux into the AIS. The remaining 39.5% of the ice flux comes from tributary basins on the east and west side of the ice shelf.

[3] The freezing point temperature of seawater decreases with increasing pressure and therefore depth. Water masses from the open ocean can enter the AIS cavity and become warmer than the local freezing temperature by moving deeper in the water column. The deep ice (~2500 m) in contact with the ocean at the southern end of the AIS is particularly susceptible to high melt, due to the large difference between ambient ocean temperatures and the *in situ* freezing point of seawater at high pressure (~−3.9°C at 34.5 psu).

[4] The circulation associated with these processes is known as the ice-pump [*Lewis*, 1985]. The resulting meltwater can mix with the ambient water forming Ice Shelf Water (ISW), which is more buoyant than the ambient water and can rise under the ice shelf. The increase in the local freezing temperature may then cause the ISW to become supercooled whereupon it can freeze directly at the ice shelf base and also (more effectively) as small frazil crystals in the water column that may later accrete to the base of the ice shelf. These two re-freezing processes lead to the formation of marine ice and act to both remove the supercooling effect from the ISW and cause it to increase in salinity (see Figure 2 for detail).

[5] Marine ice has been shown to occupy large distinct areas under the AIS [*Fricker et al.*, 2001], mainly in the north-west region. It is thought that a large component of the refrozen marine ice is due to accreted frazil [*Treverrow et al.*, 2010]. Recent observations suggest marine ice accretion can act to 'cement' adjacent ice streams together, thereby enhancing the ice shelf stability [*Holland et al.*, 2009; *Craven et al.*, 2009]. In particular, frazil is also thought to be important to sub-ice ocean dynamics and overall glacial ice mass balance [*Jenkins and Bombosch*, 1995; *Smedsrud and Jenkins*, 2004].

[6] Numerical modeling studies are crucial to improve our understanding of the impact of climate change on floating ice shelves and ice sheet mass balance. Determining the interactions between ice shelves and the ocean relies mainly on numerical simulations because *in-situ* observations in the polar regions, particularly beneath ice shelves, are sparse.

[1]Antarctic Climate and Ecosystems Cooperative Research Centre, University of Tasmania, Hobart, Tasmania, Australia.
[2]Institute for Marine and Antarctic Studies, University of Tasmania, Hobart, Tasmania, Australia.
[3]Centre for Australian Weather and Climate Research, a Partnership between CSIRO and the Bureau of Meteorology, Melbourne, Victoria, Australia.
[4]Australian Antarctic Division, Kingston, Tasmania, Australia.

Corresponding author: B. K. Galton-Fenzi, Antarctic Climate and Ecosystems Cooperative Research Centre, University of Tasmania, Hobart, Tas 7001, Australia. (ben.galton-fenzi@utas.edu.au)

0148-0227/12/2012JC008214

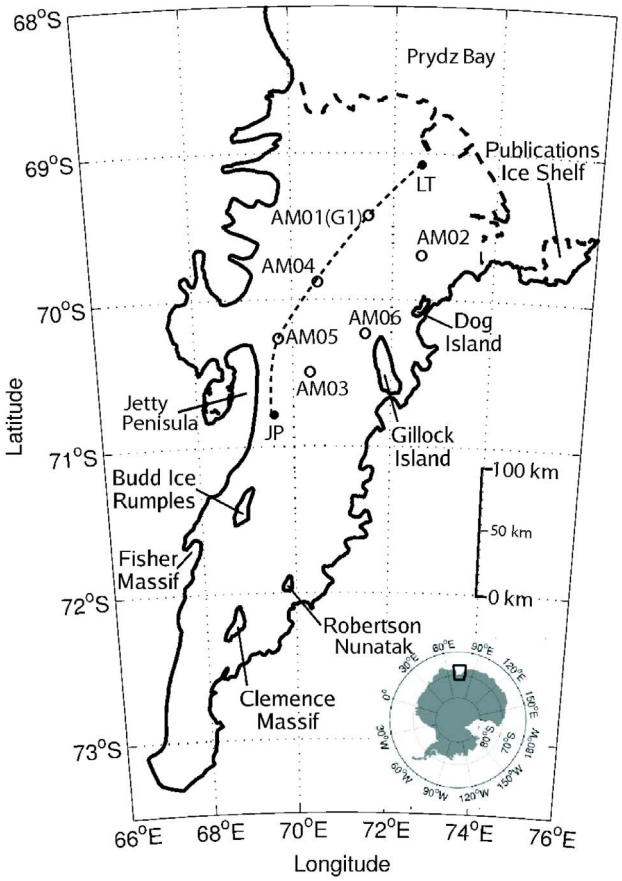

Figure 1. Study site showing important features and the flowline (dashed line) used here to compare the model results with observations. From upstream: Jetty Peninsula point (JP), where marine ice band accretion begins; AM05, AM04 and AM01 boreholes; and the "Loose Tooth" point (LT). Other borehole locations shown are AM02, AM03 and AM06.

Numerical simulations can also be used to predict the response of these mechanisms to climate change. However, most global climate models poorly resolve the continental shelf surrounding the Antarctic continent. As such, understanding the impacts of climate change on ice-ocean interaction relies on using high resolution regional models.

[7] Three-dimensional numerical ocean models have been applied to cavities under several theoretical ice shelves [*Determann and Gerdes*, 1994] and more recently to simulate real world regions such as the Filchner-Ronne Ice Shelf [*Gerdes et al.*, 1999; *Jenkins and Holland*, 2002; *Jenkins et al.*, 2004; *Grosfeld et al.*, 2001; *Grosfeld and Sandhager*, 2004], the Ross Ice Shelf [*Holland et al.*, 2003] and the AIS [*Williams et al.*, 2001, 2002]. The physics describing the basal heat and freshwater fluxes are largely understood and can be reasonably well characterized [e.g., *Hellmer and Olbers*, 1989; *Grosfeld et al.*, 1997; *Holland and Jenkins*, 1999]. However, frazil dynamics remains a complication to the processes of marine ice formation and the effect of the thermohaline circulation that occurs beneath ice shelves.

[8] The dynamics of ISW plumes have been the focus of many specialized modeling studies [e.g., *MacAyeal*, 1985; *Hellmer and Olbers*, 1989; *Jenkins*, 1991]. Frazil dynamics in ISW plumes have been studied in one-dimensional averaged models by *Jenkins and Bombosch* [1995] and *Smedsrud and Jenkins* [2004] and most recently in two-dimensions by *Holland and Feltham* [2005]. However, these models are deficient for two reasons: firstly the path that each plume follows must be known beforehand to determine the pressure at the ice shelf base; and secondly the plume is introduced between the ambient fluid and the ice shelf base and so must stay in contact with the base of the ice shelf.

[9] This paper presents results of a new model of the circulation beneath the AIS and processes that provides improved model-derived estimates of the mass balance of the AIS, and demonstrates the importance of frazil processes. The paper is arranged as follows: section 2 reviews recent observational estimates of the mass balance of the AIS; section 3 describes the model formulation and experiments; section 4 presents results and evaluates the ability of the model to reproduce the magnitude and spatial patterns of basal melting and freezing on the underside of the AIS, and section 5 presents the results of the experiments that test the impact of including a dynamic frazil model. Conclusions are presented in section 6.

2. Review of Amery Basal Mass Balance Estimates

[10] An important aspect of this study is the comparison between the estimates of the basal melting and freezing derived from the ocean modeling and those inferred from other studies of the mass balance of the AIS. We briefly discuss the widely varying estimates of net basal mass loss from published glaciological and oceanographic analyses, before presenting the results from our main reference simulation and comparing them with previous modeling studies.

[11] The major components of ice shelf mass balance are the flux of ice entering from the grounded ice sheet, snowfall and ablation on the upper surface, basal melting and freezing, and the calving of icebergs. The AIS is assumed to be in approximate mass balance [*King et al.*, 2009; *Allison*, 1979]. However, two recent glaciological studies of AIS mass balance provide three conflicting estimates of the net basal ice loss: 51.5 ± 9.6 Gt year^{-1} and 46.4 ± 6.9 Gt year^{-1} (inferred using two different methods in *Wen et al.* [2010]) and 27 ± 7 Gt year^{-1} [*Yu et al.*, 2010]. The values of 51.5 ± 9.6 Gt year^{-1}[*Wen et al.*, 2010] and 27 ± 7 Gt year^{-1} [*Yu et al.*, 2010] were derived using similar values for net accumulation over the AIS and for losses via iceberg calving. The estimate of ice flux across the AIS grounding line in *Wen et al.* [2010], based on that from *Wen et al.* [2008], is considerably different from the ice flux used in *Yu et al.* [2010]. These flux estimates are based on the same ice shelf/sheet horizontal velocity data, so the differences arise from the ways ice thicknesses at the AIS grounding line are estimated. The major mass balance components of the AIS from the flux estimates are summarized in Table 1.

[12] The remaining value from *Wen et al.* [2010] (46.4 ± 6.9 Gt year^{-1}) is an estimate of the net basal mass loss which comes from a gridded computation of ice flux divergences over the AIS, as the difference between the total basal

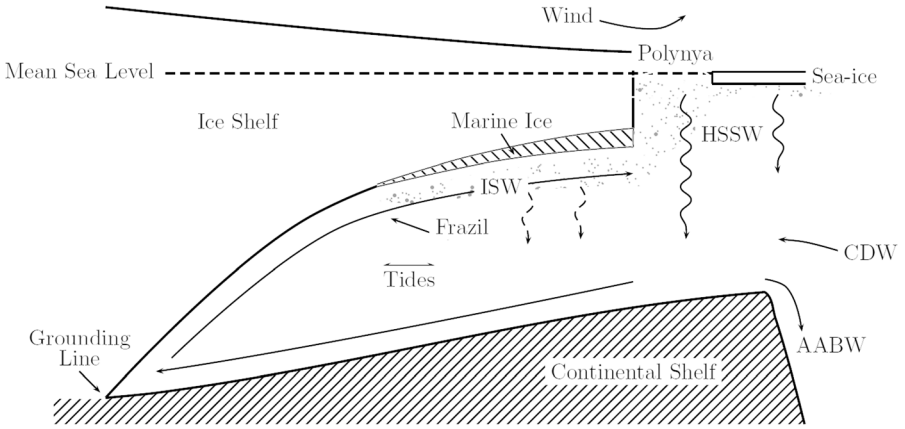

Figure 2. Schematic of an ice shelf and the 'ice-pump' mechanism (illustrated using the straight and curved lines). An inflow of Circumpolar Deep Water (CDW) can mix with the product of sea-ice formation (solid curved lines), such as High Salinity Shelf Water (HSSW), which can sink (typically poleward) down the continental shelf and can melt the ice sheet. Buoyant freshwater that is released during the melting process rises along the underside of the ice shelf as Ice Shelf Water (ISW) and can become locally supercooled at a shallower depth, leading to the formation of frazil (shown by the dots) and basal accretion of marine ice. The water that is created by the re-freezing process is analogous to that created by sea-ice formation (dashed curved lines). These processes are important for deep water formation processes – such as Antarctic Bottom Water (AABW) – that ventilate the abyssal oceans. The grounding line is the region where the ice shelf is in contact with the sea floor.

melting estimate of 62.5 ± 9.3 Gt year^{-1}, and the total basal freezing estimate of 16.1 ± 2.4 Gt year^{-1}.

[13] Exploration of the relative merits of the various estimates lies outside the scope of the present work, and for the purposes of this paper we assume that the actual net mass loss values lie somewhere between 27–51.5 Gt year^{-1}. The area-average net basal melt rate is 0.5–0.9 m year^{-1}, found by dividing the net mass loss from the AIS due to basal melt by the area of the ice shelf (60×10^3 km^2 [*Galton-Fenzi et al.*, 2008]). As emphasized by both *Yu et al.* [2010] and *Wen et al.* [2008], the high melt rates are concentrated in the southern region of the AIS.

[14] Oceanographic estimates of net basal melting have been made for the AIS [*Wong et al.*, 1998] using temperature and salinity fields observed during a cruise across the AIS ice front in the austral summer of 1991. Following *Foldvik et al.* [2001], the observations of temperature and salinity were used to estimate the net heat and freshwater exchange between the ocean cavity beneath the AIS and the external ocean. Using Conductivity-Temperature-Depth (CTD) measurements *Wong et al.* [1998] estimated the average net melt rate from the temperature data at 26.4 ± 8.6 Gt year^{-1} and from the salinity data at 14.7 ± 4.6 Gt year^{-1}. The fact these estimates do not agree suggests that *Wong et al.* [1998] incorrectly estimated the currents across the front of the AIS. More recent calculations of the basal melt rate from CTD measurements made at a higher spatial resolution than available to *Wong et al.* [1998] suggest a melt rate of ~46 Gt year^{-1} (H. Leffanue, unpublished; from 2000/01 Aurora Australis cruise data). This estimate also accounted for the heat required to warm the glacial ice from its interior temperature to the local melt temperature. It is clear that the oceanographic estimates are sensitive to the spatial resolution that can be obtained across the front of ice shelves. CTD sections may miss part of the narrow bands of outflowing ISW and inflowing High Salinity Shelf Water (HSSW), leading to an incorrect estimate of net basal melting.

[15] Net basal melting estimates derived from salinity can also be corrupted as salinity sensors can become fouled with frazil crystals and/or the bulk salinity is artificially enhanced by not measuring the freshwater component of suspended frazil. There are direct observations of frazil at depths from the surface to 125 m at the west side of the front of the AIS [*Penrose et al.*, 1994]. From the amount of supercooling present in the water, *Penrose et al.* [1994] calculated a frazil volume fraction of 1.3×10^{-3}, or about ~1.2 kg per m^3 of seawater (assuming an ice density of 920 kg m^{-3}). Depth sounding measurements during the 2000/01 cruise also showed a strong return echo at about 200–300 m below the surface, in a region where the bathymetry is known to be deeper than 500 m (M. Rosenberg, ACE CRC, personal communication, 2007). The strong return echo was attributed

Table 1. Recent Estimates of the Various Mass Balance Components (in Gt year^{-1}) for the AIS[a]

Component	Wen et al.	*Yu et al.* [2010]
Net accum. on ice sheet (A_c)	84.8 ± 4.2[b]	87.2 ± 2.9
Ice flux across GL (F)	88.9 ± 8.9[b]	64.2 ± 3.2
Catchment mass balance (A_c-F)	−4.2 ± 9.8[b]	22.9 ± 4.4
Net accum. on AIS (A_{ais})	9.8 ± 1[c,d]	10.8 ± 1[e]
Calving rate (C)	47.2 ± 3.6[c]	48 ± 4.5
Inferred basal melt (F + A_{ais}-C)	51.5 ± 9.6[c]	27 ± 7

[a]Catchment mass balance is calculated as the difference between the net accumulation over the catchment area of the ice sheet (A_c) from the ice flux (F) across the Grounding Line (GL). Net basal melt is the difference between the sum of F and the AIS accumulation (A_{ais}) and the calving rate (C).
[b]From *Wen et al.* [2008].
[c]From *Wen et al.* [2010].
[d]Modified version from *Giovinetto and Zwally* [2000].
[e]From *Vaughan et al.* [1999].

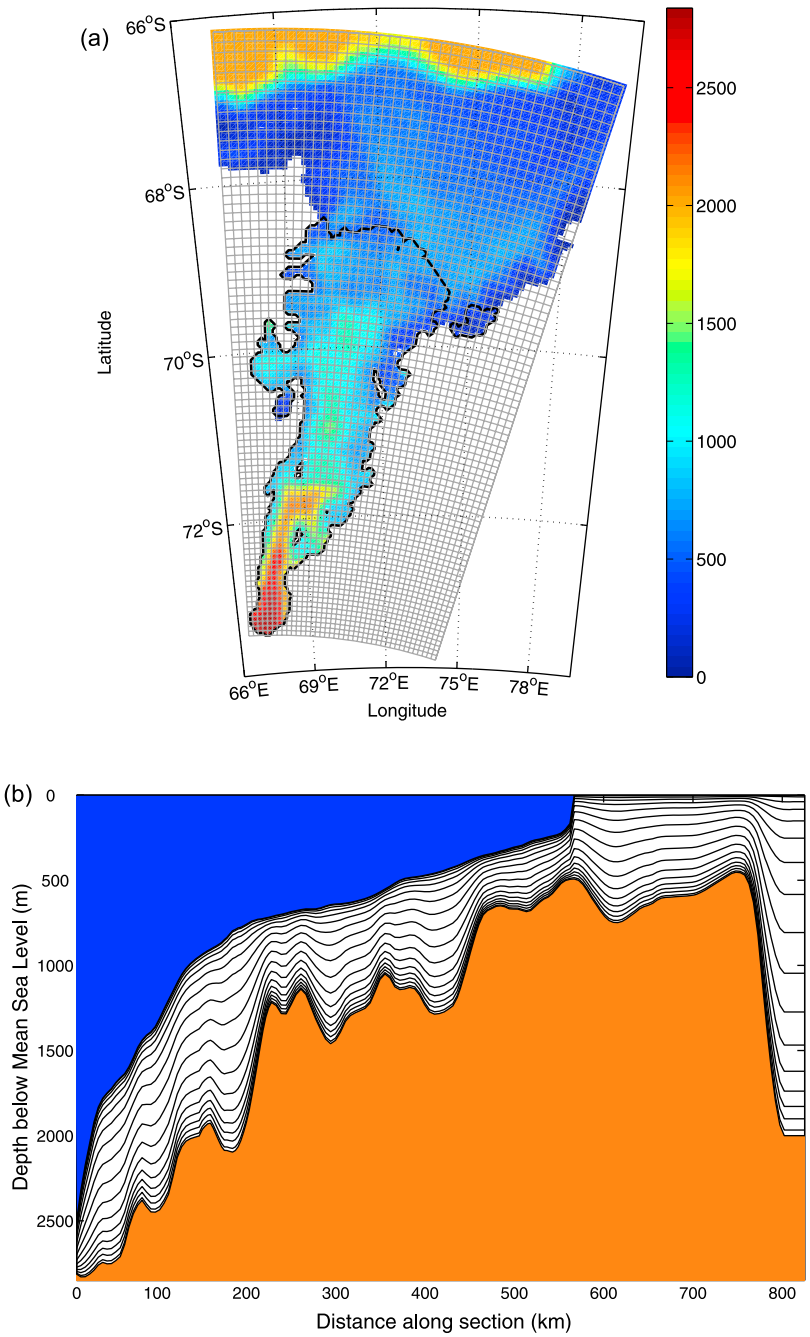

Figure 3. (a) Horizontal grid showing every second grid cell. Resolution is 3.1 km at the southern boundary and 6.9 km at the northern boundary. (b) Vertical profile along the channel centerline showing the spacing of the 16 vertical layers.

to the density contrast between water without frazil overlying water with frazil.

3. The Amery Ice Shelf Ocean Model

[16] The three-dimensional Regional Ocean Modeling System (ROMS) is a finite-difference implementation of the Reynolds-averaged Navier-Stokes equations, under the hydrostatic and Boussinesq assumptions, using a split-explicit time-stepping scheme requiring special treatment and coupling between barotropic (fast) and baroclinic (slow) modes [*Shchepetkin and McWilliams*, 2005]. ROMS has a free surface and uses a terrain-following vertical s-coordinate system controlled by the applied surface pressure, which has been adapted [*Dinniman et al.*, 2003] to allow the coordinates to follow the ice shelf draft (see Figure 3b). The model domain (Figure 3) covers the AIS and Prydz Bay, extending to an open northern boundary at 66°S at its northernmost extent. The coast and AIS grounding line of the model is a closed free slip wall and the straight eastern and western boundaries are open to the ocean but are otherwise closed. The horizontal grid is an orthogonal polar projection that was

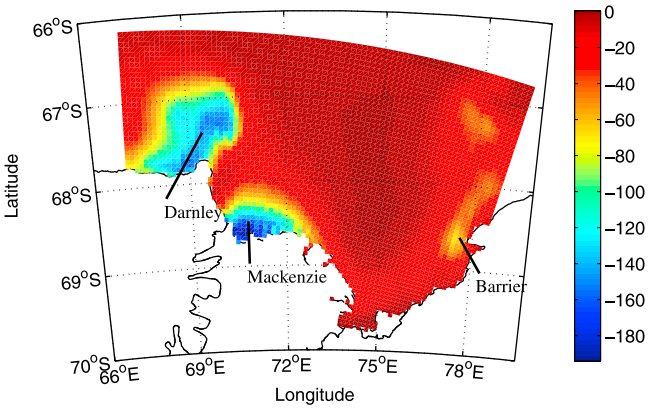

Figure 4. Winter snapshot of the surface heat flux (W m^{-2}) showing the strong effect of the Darnley, Mackenzie and Barrier polynyas. The salt and heat fluxes during active sea-ice formation are derived from the Special Sensor Microwave Imager (SSM/I) [*Tamura et al.*, 2008] which, during the summer months, are supplemented with fluxes from NCEP-2 [*Kanamitsu et al.*, 2002].

developed to minimize wasted cells due to land masking, especially to the south. The horizontal grid resolution ranges from ~3 km near the southern boundary to ~7 km near the northern boundary.

[17] There are 16 vertical levels that are concentrated towards the top and bottom of the model domain (see Figure 3). The thickness of the top model layer ranges from 0.72 m over the shallows to 28.69 m over the deep ocean. The interpolated geometry (bathymetry and ice draft) [*Galton-Fenzi et al.*, 2012, 2008; *Maraldi et al.*, 2007] represents a significant advance over previous modeling studies of the region [*Williams et al.*, 2001, 2002; *Hemer et al.*, 2006]. The bathymetry was smoothed with a modified Shapiro filter that was designed to selectively smooth areas where the changes in bathymetry are large with respect to the total depth [*Wilkin and Hedström*, 1998]. A similar filter was used for the ice draft. Most of the smoothing was on the sea floor and there was less smoothing required for the ice draft and over the shelf break. The mean modulus of the slope over the entire model domain was reduced from 1.1% to 0.9%.

[18] The choice of mixing and advection schemes follows the choices that were used by *Dinniman et al.* [2003, 2007] for studies of the shelf seas near the Ross Ice Shelf. The Laplacian horizontal mixing of tracers uses a diffusivity of 5 m^2 s^{-1}. A background value (100 m^2 s^{-1}) of explicit horizontal momentum mixing was required for stability. Quadratic boundary stress, with a coefficient of 2.5×10^{-3} (non-dimensional), was applied as a body force over the bottom layer and that part of the surface layer in contact with the ice shelf. The vertical momentum and tracer mixing used the K profile parametrization (KPP) mixing scheme [*Large et al.*, 1994], including the use of a surface mixed layer.

[19] The initial conditions of the seawater properties are horizontally-uniform temperature and salinity with a vertical profile that increases linearly from 34.35 psu at the surface to 34.65 psu at the bottom, and a temperature that decreases linearly from −1.85°C at the surface freezing point to −2.05°C at the bottom. The model uses 300 seconds for the baroclinic time-step and 7.5 seconds for the barotropic time-step.

[20] The melting and freezing formulation uses the full three-equation formulation outlined in *Hellmer and Olbers* [1989] and *Holland and Jenkins* [1999]. The frazil formation part of the model is based on the plume model of *Holland and Feltham* [2005, 2006], with differences due to the application in a three-dimensional ocean model and allowing for the growth of frazil in saltwater (outlined in Appendix A). ROMS allows for the addition of extra tracers and then treats the advection and diffusion of frazil. Five frazil size classes with diameters of 0.1, 0.3, 0.6, 0.8 and 1.0 mm are used. All experiments are initialized with a zero concentration of frazil. Supercooled water is seeded with small concentrations of frazil equally across all size classes. The growth rate is scaled to consider the effects of salt exchange, which is an advance on previous studies [e.g., *Holland and Feltham*, 2006].

[21] The frazil rise velocity is calculated using a piecewise continuous function (Appendix A, equation (A14)) [*Morse and Richard*, 2009]. Preliminary studies showed the stability limits imposed on the frazil growth (melt) rate (i.e., not to exceed the amount of supercooling (heating) during a single time-step) are important only during the initial spin-up of the model, otherwise the frazil model behaves dynamically and allows interactions between size classes to occur within the model time-step. To minimize the shock of high frazil growth during the initial spin-up stage, the frazil growth rate was ramped up over one year.

[22] Brine rejection during the formation of ice in polynyas is considered to be very important in the creation of dense water that can drain underneath the ice shelf, melting the underside. The dense water that is created as a result of these processes also has the potential to lead to the production of Antarctic Bottom Water [*Williams et al.*, 2008]. The response of the ocean to coastal polynyas has been investigated using ocean models that include sea-ice dynamics [*Marsland et al.*, 2004; *Stössel et al.*, 2007]. Recent modeling highlights the importance of small scale features, such as grounded icebergs that aid the formation of polynyas, leading to localized enhanced dense water production [*Kusahara et al.*, 2010]. Coastal polynyas and icebergs are of critical importance to the production of dense water but are often poorly resolved or are not parameterized in models.

[23] As such, for the purpose of this study, open ocean boundary conditions are prescribed surface fluxes based on ice concentrations from a climatology derived model using Special Sensor Microwave Imager (SSM/I) observations [*Tamura et al.*, 2008] (e.g., see Figure 4). These estimates are useful during the time of active sea-ice growth and represent the brine formation from polynyas especially well. The surface salt flux in *Tamura et al.* [2008] is calculated from the estimated ice production rates over the freezing period from March to October by assuming that all of the heat loss at the surface is used for ice formation. The ice production rate is converted to a surface salinity flux: an annual ice production of 1 m corresponds to salinity flux of 21.7 kg m^{-2} $year^{-1}$, assuming a water and thin ice salinity of 35 and 10.85 psu, respectively [*Martin and Kauffman*, 1981]. During summer, the *Tamura et al.* [2008] data are supplemented with open-water heat and salt fluxes using monthly climatologies from NCEP-2 [*Kanamitsu et al.*, 2002].

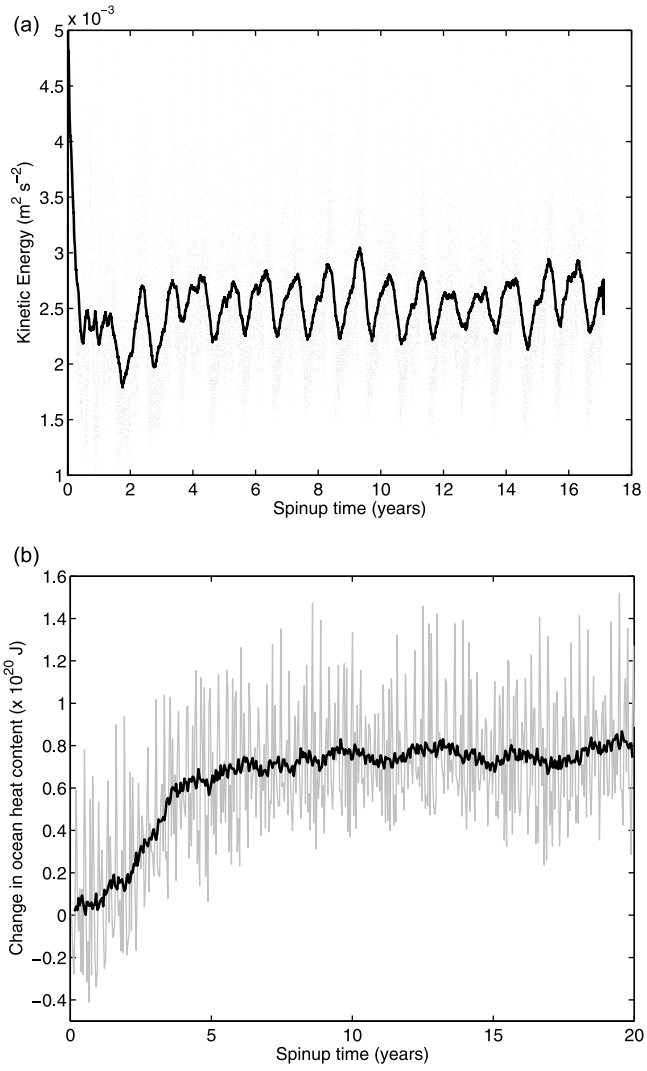

Figure 5. Time histories of (a) the average model kinetic energy and (b) the change in heat content for the ocean cavity beneath the AIS. The large variability (grey) is predominantly due to tidal oscillations. The time history also shows a strong seasonal cycle and inter-annual variability (black line). The grey dots are 4.2 hourly model output and the black line is a smoothed version using a 30 day moving average. Between 10 and 20 years there is still a slight increase in the total heat content beneath the ice shelf of 2.4×10^{17} J year^{-1}.

[24] The timing of the maximum heat flux in winter is closely associated with the maximum wind strength computed from NCEP-2 fields. A wintertime snapshot of the ocean region not covered by ice shelves shows the strongest heat fluxes occur at the Cape Darnley, the Mackenzie and Barrier polynyas, located within the domain of the model (see Figure 4). The Cape Darnley and Barrier polynyas may be enhanced by the position of blocking grounded icebergs in the region. Together, these three polynyas produce a volume of ice comparable to the Ross polynya [*Tamura et al.*, 2008]. Note that the Cape Darnley polynya (181 ± 19 km^3) is the second most productive polynya around Antarctica, the Barrier (80 ± 19 km^3) is seventh and the Mackenzie (68.2 ± 5.8 km^3) is tenth [*Tamura et al.*, 2008].

[25] Lateral ocean boundaries for tracers and horizontal velocities in the model are relaxed to climatology from the ECCO2 model [*Menemenlis et al.*, 2008; *Wunsch et al.*, 2009]. Lateral boundary fields (potential temperature, salinity and currents) on the open boundaries are relaxed to monthly climatologies. The time scales of the linear relaxation are 30 and 2 days for inward and outward advection velocities, respectively. Frazil concentrations are relaxed to zero concentration over 10 days, which prevents unwanted frazil from building up within the model domain. No sponge layer, or region of increased horizontal viscosity near the open boundaries, was used. ECCO2, which is a data assimilating global model with realistic air-sea interactions and sea-ice processes, has been used in a form to simulate the circum-Antarctic ice shelves [*Losch*, 2008].

[26] Recent studies have highlighted the importance of tides on the basal melting of ice shelves [e.g., *Mueller et al.*, 2012]. The tidal amplitudes and phases are calculated using a non-standard ROMS subroutine based on tidal information from the National Oceanography Centre (NOC), Liverpool [*Murray*, 1964] and modified to be included within ROMS, yielding a standard tidal prediction. The combination Flather/Chapman sea surface elevation conditions were used with the barotropic tidal currents added to the boundary currents.

[27] The decay times of initial transients in ice shelf-ocean modeling studies are varied. Published descriptions of model spin-up procedures often lack sufficient detail to reveal the rate of the convergence of the solution. Simplified studies by *Holland et al.* [2008] use 10 years as spin-up time. Models of the open ocean region of the Ross Sea have used 5 years spin-up time [*Dinniman et al.*, 2007]. Realistic ice shelf-ocean interaction studies use 10 years as an appropriate spin-up time [e.g., *Darelius et al.*, 2009; *Holland*, 2001].

[28] During model spin-up, bulk measures, such as basin-averaged kinetic energy, are common methods to monitor the approach of the model simulation to an approximate steady state. The average time history of kinetic energy (Figure 5) shows that the model has reached approximate steady state after about 4 years of integration, in agreement with modeling studies by *Dinniman et al.* [2007] using ROMS with similar grid resolution and boundary forcing characteristics.

[29] However, because the model used here is primarily designed to investigate ice-ocean interactions, diagnosing the appropriate integration timescale should also include an analysis of the evolution of the tracer fields. The time history evolution of the ocean heat content ($\mathcal{HC}$) over time is given as,

$$\mathcal{HC} = \sum_{i,j,k} \Delta\mathcal{V}_{i,j,k} T^K_{i,j,k} c_p \rho_{i,j,k} \tag{1}$$

where $\Delta\mathcal{V}$ is the tracer control volume, T^K is the temperature in °K, c_p is the specific heat capacity of polar seawater (3974 J kg^{-1} K^{-1}) and ρ is the density (kg m^{-3}) for each cell, i, j and k.

[30] Figure 5b shows the time history of heat content for the total model relative to the initial heat content. The open ocean quickly adjusts to the boundary conditions. The

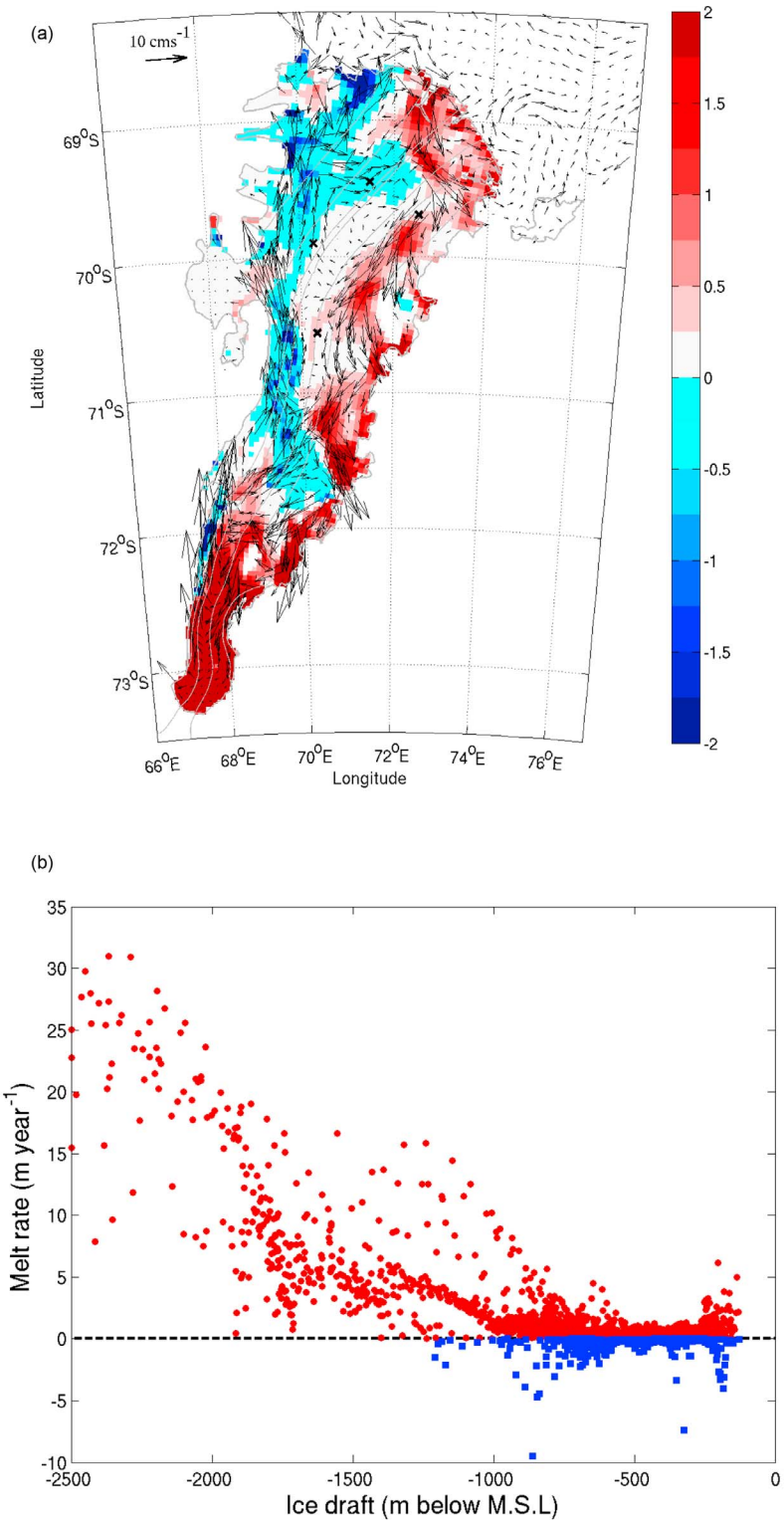

Figure 6. (a) The annual averaged pattern of melting (positive; m ice year^{-1}) and freezing (negative) superimposed with depth average currents, and (b) the melt rate from Figure 6a plotted against ice draft thickness. Crosses in Figure 6a are the borehole locations shown in Figure 1.

evolution to steady state in the total model heat content suggests that the tracers reach approximate steady state at about the same time scale as the kinetic energy, i.e., after about 5 years. The dominant mechanism driving changes in the ocean heat content is primarily correlated with the tidal oscillations. As the prescribed heat transfer primarily depends on the velocity of the water adjacent to the base of the ice shelf, tidal currents enhance the melting/freezing

Table 2. Summary of Local Estimates of Melt and Freeze Compared to the Reference Model Results[a]

Study	Method	Rate (m ice year^{-1})
Melt Rate Near Southern Grounding Zone		
Reference model	Modeling	23 (32)
Wen et al. [2010]	Flux boxes	25.0 ± 4.0
Yu et al. [2010]	Flux gates	10.4 ± 2.6
Wen et al. [2007]	Flux boxes	23.5 ± 3.5
Rignot and Jacobs [2002]	Flux gates	31 ± 5
Freeze Rate Near 70°E,70°S		
Reference model	Modeling	1.2 (4)[b]
Wen et al. [2010]	Flux boxes	0.8 ± 0.5 (2.4 ± 0.4)
Craven et al. [2009]	Drilling/Boreholes	1.1 ± 0.2–1.3 ± 0.2
Wen et al. [2007]	Mass balance	1 ± 0.5

[a]The model values are an area average with size similar to that used in observational studies. The bracketed values are the highest rates observed in the region.

[b]The maximum refreezing is calculated between Jetty Peninsula and AM05.

rates, leading to the large fluctuations in ocean heat content associated with the spring/neap tides (seen as the grey line in Figure 5b). Closer examination shows that the influence of the seasonal cycle is strongest beneath the ice shelf near the front and diminishes with distance towards the southernmost part of the cavity (not shown). However, the residence time of seawater in the cavities beneath ice shelves is also important when considering the spin-up of an ice shelf ocean model. As such, simulations presented here cover a period of 20 years. Analyses are performed on monthly averages of the final 3 years of model output. Within the context of the paper, time scales shorter than one month are not considered.

3.1. Experiments

[31] Two model simulations are presented that were designed to assess the impact of frazil dynamics on marine ice accretion and ISW production in the vicinity of the AIS:

[32] 1. "Reference": the reference simulation uses the most sophisticated treatment of both the basal ice-ocean thermodynamics and frazil dynamics.

[33] 2. "Without Frazil": as for the reference simulation but without frazil dynamics.

4. Results and Discussion

4.1. Basal Melt and Marine Ice Accretion

[34] The annual averaged net loss of ice due to basal melting from the reference model is ~45.6 Gt year^{-1}. The simulated net mass loss lies well within the uncertainty of the glaciological estimate of $27 \pm 7 - 51.5 \pm 9.6$ Gt year^{-1}. The annual averaged spatial pattern of melting and freezing for the reference simulation is shown in Figure 6. The freeze rates are the sum of the contributions from both direct basal refreezing and frazil accretion. Areas of melting occur primarily along the east and south of the AIS and areas of refreezing primarily occur along the western side of the ice shelf, consistent with our understanding of the circulation patterns beneath the AIS. The observed model inflow in the east of the model domain causes areas of melting adjacent to Gillock Island that corresponds to a rise of the sea floor. The strongest regions of freezing are located in regions where the ice draft contains hollows, such as north and east of the Budd Ice Rumples, near Jetty Peninsula and near to the outflow region of the ice shelf (see Figure 1 for locations).

[35] The melting rate for each model cell beneath the AIS is shown in Figure 6b and shows that the strongest melt occurs where the ice is deepest. The maximum amount of melt that occurs in this region exceeds 30 m ice year^{-1}. A comparison of the model melt/freeze with observational estimates is shown in Table 2. The model results are in strong agreement with a study of local basal melting and freezing rates, using glaciological flux gate estimates, that show the mean melting rate near the southern grounding line is 23.5 ± 3.5 m ice year^{-1} [*Wen et al.*, 2007]. The *Wen et al.* [2007] study also showed that melting decreased rapidly downstream, and transitioned to refreezing at around 300 km from the southern extremity of the AIS, in agreement with the reference model results. Freezing rates along the Mellor, Lambert and Fisher flowbands ranged from 0.5 ± 0.2–1.5 ± 0.2 m ice year^{-1}. Estimates based on flux gate calculations yielded average melt rates of 31 ± 5 m ice year^{-1} in the region near the southern grounding line [*Rignot and Jacobs*, 2002; *Rignot*, 2002]. Recent results from direct observations showed that local freezing between Jetty Peninsula and *in-situ* borehole AM04 are an average of ~1.3 ± 0.2 m ice year^{-1} to account for the amount of marine ice encountered at borehole AM04 [*Craven et al.*, 2009]. Similarly, the average rate of accretion between boreholes AM04 and AM01 that is required to account for the observed marine ice at AM01 was found to be ~1.1 ± 0.2 m ice year^{-1} [*Craven et al.*, 2009].

[36] The area of refreezing to the south of the Budd Ice Rumples against the western model boundary does not exist in the observations of marine ice thickness [*Fricker et al.*, 2001]. East-west cross sections of the ice draft across the refreezing zone (not shown) indicate that the ice draft shoals towards the western boundary. This would mean that ISW, flowing along the underside of the western boundary, can become supercooled as it rises into the shallow part of the ice draft, causing refreezing to occur. The shallowing in the ice draft along the western boundary is likely due to the grounding line position being misplaced too far west in the interpolation of the ice draft. Future studies should investigate the robustness of the results presented here to grounding line placement and/or ice draft values. It has been shown that the reference model's ability to simulate the net basal mass loss rates and local estimates of melting and freezing compare favorably with the available observations.

[37] The ability to simulate marine ice thickness, in rough agreement with observations, is a strong test of a model's ability to simulate the basal melting and freezing rates [*Holland*, 2002]. The thickness of the marine-ice layer is estimated here by utilizing the total thickness, horizontal flow field and basal accumulation rate. This technique, based on the principle of conservation of mass, has been previously described by *Budd et al.* [1982], and applied to Antarctic ice shelves [e.g., *Determann*, 1991; *Williams et al.*, 2001] and simplified studies [*Holland*, 2002].

[38] Glaciological derived estimates of velocity and strain thinning from *Young and Hyland* [2002] are used to calculate the marine ice accretion along a flowline. The flowline

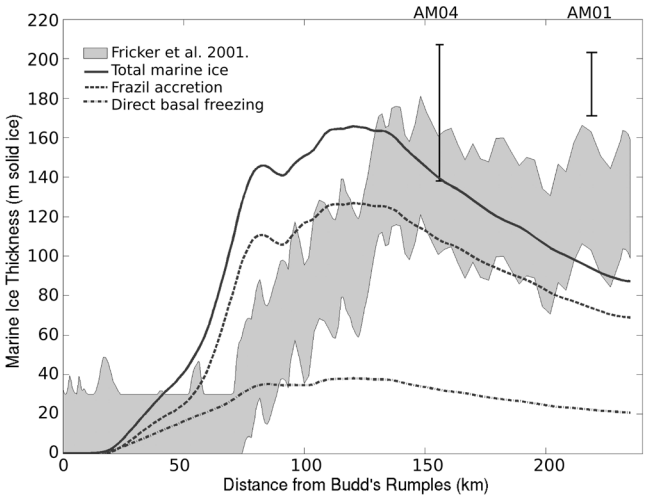

Figure 7. Estimate of marine ice thickness for the reference simulation for the ice shelf flowline that passes through boreholes at AM04 and AM01. The vertical solid line at about 100 km from JP is from direct observations through a borehole drilled at site AM04. The error in the borehole measurements represents conversion from the measured thickness to meters of solid ice equivalent. The error bars are measures of the uncertainty in estimates of the marine ice porosity. The thick shaded area is from *Fricker et al.* [2001].

used for the comparison is shown in Figure 1 as the dashed line, originating at Jetty Peninsula (JP) (see Figure 1) and passing through boreholes AM05, AM04 and AM01. The southernmost point along the flowline where the ice shelf shows zero ice accretion is at JP and was used as the starting point for the integration. Note that at AM05 measurements of the thickness of the marine ice layer were not made due to equipment problems. Marine ice thickness measurements were made at the two remaining boreholes (AM04 and AM01) that lie along approximately the same ice shelf flowline, which allows direct observations of marine ice thickness to evaluate the integration. The direct observations of marine ice thickness were converted to a consolidated ice equivalent using the appropriate marine ice porosity for each site as reported in *Craven et al.* [2009]. The marine ice thickness along the flowline from *Fricker et al.* [2001] (with estimated uncertainties of ± 30 m), are also compared with both the direct observations and the reference model results.

[39] The marine ice thickness estimates along the flowline, derived from the model's pattern of basal melting and freezing, are shown in Figure 7. The majority of the marine ice accretion is due to the precipitation of frazil. Generally, the reference model deposits marine ice closer to the Budd Ice Rumples than is suggested by the marine ice map of *Fricker et al.* [2001]. At AM04, the reference model shows marine ice thicknesses comparable to both the estimates from remote sensing and direct observation. At AM01, the reference model shows $\sim$80 m of marine ice compared to $\sim 141 \pm 30$ m of ice from *Fricker et al.* [2001] and a solid ice equivalent of 187 ± 16 m of consolidated ice from the borehole measurements.

[40] As the ice shelf flowlines run roughly parallel with the direction of the frazil laden ISW, most of the offset can be explained by frazil being deposited from the water column about 40–50 km too far south along the flowline, suggesting slight premature settling of frazil from the ISW plume. Even considering this offset, the model still underestimates the marine ice at AM01 by about 50 m. However, it is remarkable that a frazil model with 5 frazil size classes can lead to approximately the observed spatial pattern and magnitude of accretion. The low deposition at the northern part of the flowline is likely due to the model's inability to model the flow within porous marine ice. Observations have shown that up to 100 m of the lower part of the marine ice beneath the AIS may be in hydraulic connection with the ocean and is also much rougher than in regions of melt [*Craven et al.*, 2009].

[41] The results from the reference experiment are summarized in Table 3 and compared with previous modeling studies and the observations. In previous modeling studies, the simplest model used several two-dimensional overturning configurations representative of the AIS cavity [*Hellmer and Jacobs*, 1992]. Results from that study indicated a mean melting rate of 0.65 m ice year^{-1}, equal to the removal of 23 Gt year^{-1} of basal ice using the much smaller ice shelf area utilized in their model. *Williams et al.* [2001] used a three-dimensional numerical ocean model to simulate the ocean cavity beneath the AIS with two different boundary conditions for the barotropic flow at the ice front. The two simulations gave total basal melt rates of 5.8 Gt year^{-1} and 18.0 Gt year^{-1}, respectively. Both models showed basal freezing of several Gt year^{-1}.

Table 3. Comparing the Observed and Simulated Annual Averages of Freshwater Flux (FWF), Net Basal Mass Loss (BML) From Ocean Models Used to Simulate the Cavity Beneath the AIS[a]

Study	Area ($\times 10^4$ km^2)	Basal Melt Rate (m ice year^{-1})	FWF (mSv)	BML (Gt year^{-1})
Reference Model	6.2	0.74	1.45	45.6
Hellmer and Jacobs [1992]	3.5	0.65	0.73	23
Williams et al. [2001]	5.6	0.11–0.35	0.20–0.62	5.8–18
Hellmer [2004][b]	5.6	0.35	0.55	17.65
Glaciological observations[c]	6.0	0.5–1.0	0.8–1.6	27–51.5
Oceanographic observations[d]	6.0	0.7	1.5	46

[a]An ice density of 916 kg m^{-3} is assumed, except for *Hellmer* [2004] where 917 kg m^{-3} was used. 1 milliSverdrup (mSv) = 1000 m^3 s^{-1}.
[b]Results are from a circum-Antarctic ocean model.
[c]Range from *Yu et al.* [2010] and *Wen et al.* [2010].
[d]Leffanue (unpublished; from 2000/01 Aurora Australis cruise data).

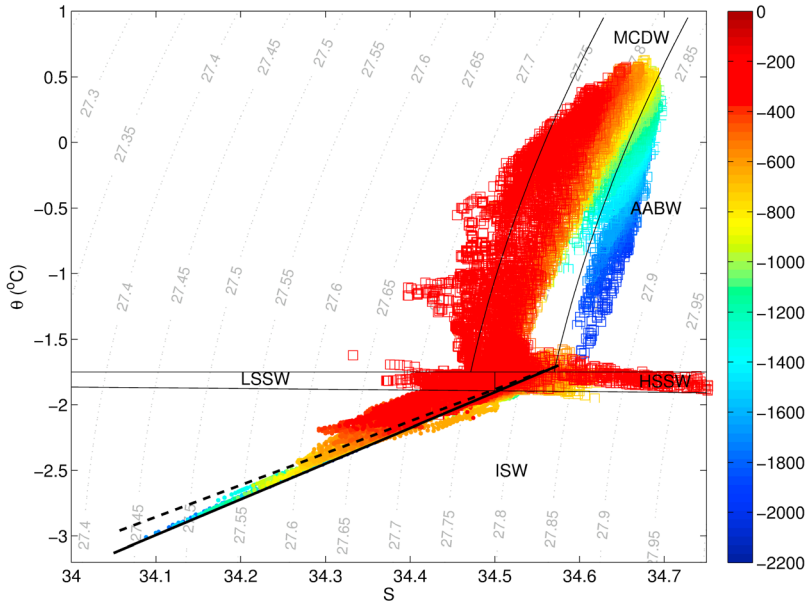

Figure 8. Summertime distribution of potential temperature (θ °C) and salinity (S psu) for every second model grid cell in the open ocean (squares) and for the ocean cavity (circles) below 200 m beneath the open ocean surface. The color scale shows the depth for each cell. The grey dotted lines are potential density contours; the thin solid lines define the water masses. The thick lines in the ISW show the dilution relation when ice melts/freezes in seawater, without considering the heat flux into the ice shelf (dashed solid line) and with the heat flux into the ice shelf (thick solid line) [*Gade*, 1979]. Acronyms are defined in the text, except Low Salinity Shelf Water (LSSW).

[42] These previous simulations varied widely from our reference simulation on the choice of model type, cavity geometries, and forcing fields. The models are all similar in as much as the ice-ocean boundary conditions are variations of the three-equation basal ice-ocean boundary conditions outlined in Appendix A. In all cases, net basal mass loss estimates from previous models are much lower than suggested by the observations. The good performance of the reference model is attributed to improved cavity geometry, the inclusion of realistic seasonally varying boundary conditions, and the inclusion of both frazil and tides.

4.2. Oceanic Circulation and Water Masses

[43] The AIS basal melt/freeze is controlled by the oceanic temperature and salinity. The distribution of θ and S below 200 m is shown in Figure 8. The plot shows every second cell from the model for the open ocean (squares) and the ocean cavity (circles). The profiles of θ and S in the AIS cavity follow a classic melt/freeze dilution line, first proposed by *Gade* [1979] and here called the 'Gade Line'. The dashed line assumes no heat is required for warming the glacial ice to the local freezing point before melting can occur and the solid line assumes that the glacial ice is first warmed (from ~ -20°C) to the local freezing point before it is melted. The water masses driving the melting at the deepest parts of the ocean cavity beneath the AIS originate from winter sea-ice formation processes. The Gade Line relationship between $\theta - S$ shows that those waters are saltier than the waters that drive melting at the shallower parts of the cavity.

[44] The general summertime circulation seen in the model agrees with the results of previously published work. Figure 9 shows the spatial patterns of model horizontal currents and θ (left panels) and S (right panels) for the s-layer below the surface layer (top panels) and the bottom s-layer (bottom panels). The large-scale circulation in Prydz Bay is characterized by a strong inflow of MCDW into Prydz Bay from the eastward flowing offshore current [*Nunes Vaz and Lennon*, 1996]. A narrow westward flow along the continental shelf break has also been observed [*Wong et al.*, 1998] and offshore, just to the north of the shelf break is characterized by eastward flow, which has been associated with the southern extent of the Antarctic Circumpolar Current [*Wong et al.*, 1998; *Meijers et al.*, 2010].

[45] MCDW is recirculated across the front of the AIS as part of the Prydz Bay gyre. The subsurface layer shows that ISW is following the coastline, in agreement with measurements made during the BROKE-west survey that showed a signal of outflowing ISW to the western side of the Prydz depression [*Meijers et al.*, 2010]. The water exiting the model domain to the west occurs in two regions: 1) along the coast, as a coastal current; and 2) as a strong current along the continental slope, after exiting from the Prydz Bay channel. The coastal current exits the model domain carrying HSSW that has been modified by the ISW outflow.

[46] The dominant circulation beneath the AIS ($\sim$10 cm s^{-1}) is a clockwise buoyancy driven circulation pattern primarily characterized by inflowing HSSW during wintertime and the outflow of ISW, linked by two stable and seasonally

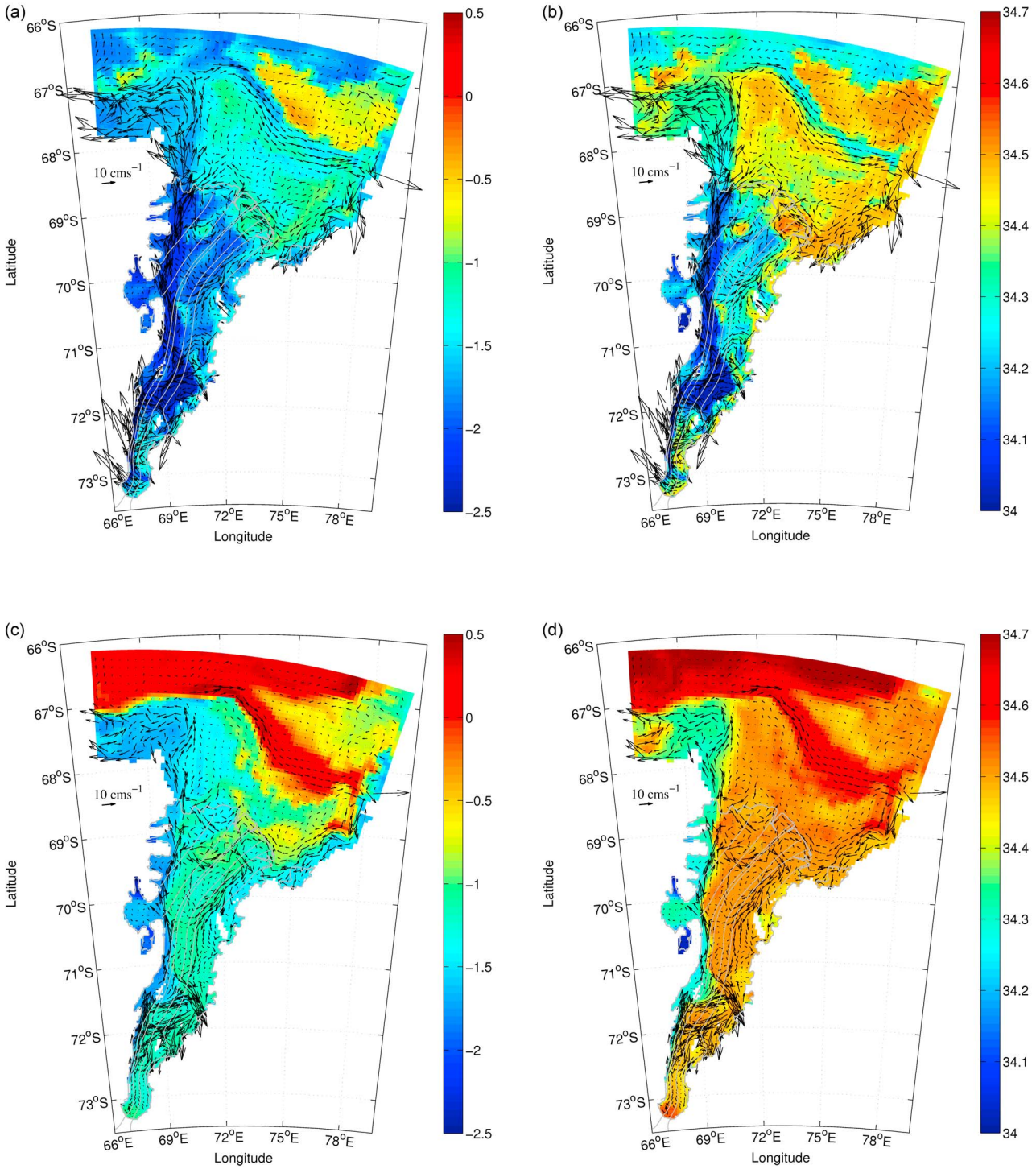

Figure 9. (left) Summertime potential temperature (θ°C) and (right) salinity (S psu) for (a, b) the s-layer below the surface layer and (c, d) the bottom layers. Currents in these layers are also shown. Glacier flowlines and the calving front are indicated by the thin grey lines.

persistent recirculation features, one in the region to the northwest of Gillock Island and the other to the southeast of the Budd Ice Rumples. The main inflow of HSSW is near the center of the front of the AIS, near the Loose Tooth region (see Figure 1 for location) [*Fricker et al.*, 2005], and comprises water that is recirculated from within the Prydz Bay gyre and the coastal current. A weaker inflow region also occurs in the east that combines with the main inflow site and is driven against the east boundary leading to strong basal melting, along the eastern side of the AIS. A third variable recirculation feature is seen in the northwest most region of the AIS and is present during summer and

Table 4. Model Estimates of the Various Basal Mass Balance Components for the AIS[a]

Model	Net	Melt	Freeze
Reference	45.6	50.9	5.3
Without Frazil	50.9	53.0	2.1
Flux estimates[b]	27–51.5	-	-
Grid-based estimate[c]	46.4 ± 6.9	62.5 ± 9.3	16.1 ± 2.4
Marine ice flux[d]	-	-	∼5

[a]Net = Melt-Freeze (Gt year^{-1}). The total refreezing for the reference experiment is comprised of 1.64 Gt year^{-1} of direct basal refreezing and 3.62 Gt year^{-1} of frazil accretion.
[b]From *Wen et al.* [2010] and *Yu et al.* [2010].
[c]From *Wen et al.* [2010].
[d]As described in the text.

influences both outflowing ISW and brings warmer waters into contact with the front part of the AIS (see section 4.4).

[47] The outflowing ISW, which originates from deep in the AIS cavity, is primarily trapped against the western boundary as it flows towards the open ocean. During winter the outflowing ISW bifurcates approximately 100 km from the open ocean, leading to two plumes of ISW, that rejoin in Prydz Bay when encountering the coastal current that flows across the front of the AIS. The coherent plumes of ISW are laden with frazil at concentrations as high as ∼1 kg m^{-3}. The circulation in the bottom layer shows a recirculation feature that is constrained by the position of the Budd Ice Rumples (see Figure 1 for location). The upper layer shows that the northward flowing ISW is not connected with the bottom flow and is diverted to the west of the Budd Ice Rumples before again continuing northward along the western boundary.

4.3. The Effect of Frazil on Ice Shelf Mass Balance

[48] To test the impact of frazil on the circulation and mass balance of the AIS, a comparison between the reference experiment (with frazil) and an experiment without frazil, is presented in this section. The basal melt rates can be indirectly affected by the presence of frazil due to modification of the water properties, particularly the temperature. The net melting rate in the reference model (with frazil) is 5.3 Gt year^{-1} lower than the model without frazil. The reference model has much higher rate of freezing than the model without frazil (see Table 4). The rate of marine ice accretion in the reference model is much lower than that of *Wen et al.* [2010] but in near agreement with an independent estimate (details to be presented elsewhere) of marine ice accretion. The latter estimate was calculated from the peak integrated flux of marine ice, using ice shelf velocities [*Young and Hyland*, 2002] and marine ice thicknesses [*Fricker et al.*, 2001] and indicates a freezing rate of about 5 Gt year^{-1}.

[49] The lower melting rate in the reference model simulations is attributed to the strong difference in the basal melting and freezing patterns (see Figure 10). The water masses that enter beneath the cavity in both the reference

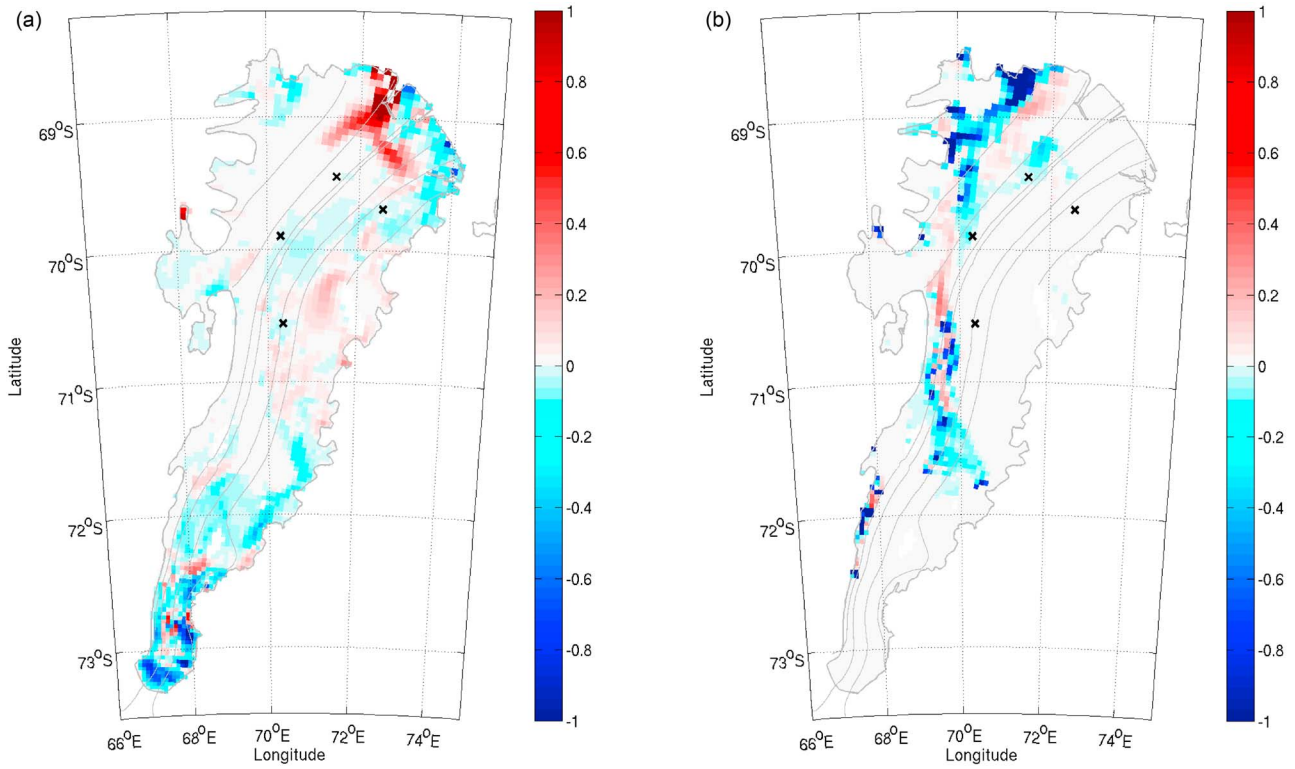

Figure 10. The effect of including frazil on (a) basal melting and (b) freezing (m ice year^{-1}) on the underside of the AIS from the differences between the reference model and the model without frazil dynamics. The colors should be interpreted as positive indicates the reference model melts more than the model without frazil (Figure 10a) and positive indicates the reference model has higher rates of accretion than the model without frazil (Figure 10b). Crosses indicate the borehole locations shown in Figure 1.

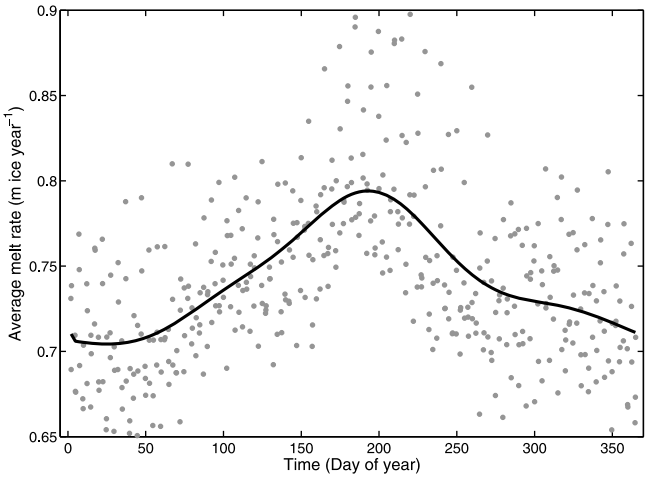

Figure 11. The seasonal variation of the area averaged melt rate (m ice year^{-1}), averaged for each month (black line). The raw 2.5-day model output shows tidal aliasing (grey dots).

model and the model without frazil have about the same amount of heat. The lower melting rate shown in the reference model is attributed to the enhanced vertical mixing of supercooled water with the ambient water due to the associated brine rejection process associated with frazil formation. Consequently, the water masses that reach the deeper parts of the cavity under gravity are slightly cooler than the same water masses in the model without frazil due to vertical entrainment processes. The reduction that this effect has on the basal melting processes is shown in Figure 10a. The model without frazil has higher rates of melting near the southernmost parts of the AIS.

[50] The growth of frazil increases the salinity of the ocean which can act to destabilize the ISW plume, as the frazil precipitates from the ocean. Frazil is a much more efficient method of removing supercooling and so the reference model produces ISW that is saltier and warmer than the model without frazil. The model without frazil shows a spreading plume of ISW that covers a larger area at the base of the AIS, which also acts to insulate the cavity from the melting effects near the front.

4.4. Seasonal Variability of Melt/Freeze and Circulation

[51] The area-averaged seasonal cycle of net basal melt rate is shown in Figure 11. The net melt rate exhibits a strong seasonal cycle with the highest mean rates, of $\sim$0.8 m ice year^{-1}, occurring in July. The high variability in the area-averaged melt rate of $\sim\pm$0.1 m ice year^{-1}, shown by the grey dots, is due to (aliased) tidal oscillations.

[52] Figure 12 shows the melt/freeze standard deviation and velocity variance ellipses, indicative of the seasonal variability. Beneath the ice shelf, a strong seasonal cycle is a characteristic of the model and is stronger towards the open ocean. The western boundary current of ISW (lighter colors) is a stable feature on seasonal time scales. The variability of the basal melt rates is $\sim\pm$2 m ice year^{-1} in regions along the front of the AIS and at regions along the eastern boundary. The major variability in the currents occurs beneath the ice shelf within 100 km of the open ocean. Borehole sites AM01 and AM02 are within the region of high current variability, which is reflected in the seasonal cycles of temperature and salinity, compared to borehole sites AM03 and AM04.

[53] The AM01 borehole is located at a region of primarily inflowing waters that exhibit high seasonal variability (black ellipses). Potential temperatures and salinities in the ice shelf cavity are roughly out of phase over a seasonal cycle at AM01 and AM02, with temperature falling as salinity rises, and *vice versa*. This is an indicator that inflow of HSSW dominates the average properties of the ocean near the front of the AIS, which forms in large quantities in the regions of both the Mackenzie and Barrier polynyas. The water masses beneath the AIS are rarely warmer than the surface freezing point. HSSW is the main water mass that drives melting of the deep ice in the southern region of the AIS. Although the less dense water masses do not penetrate far into the cavity, a large proportion of the cavity volume lies close to the ice front where seasonal variations are strong. Near the front of the ice shelf, exchange with the open ocean also occurs during the summer months when the average temperature of the cavity rises and the average salinity falls. This reflects the mixture of Low Salinity Shelf Water (LSSW), MCDW and some surface water that enters the cavity along with HSSW during the summer period. Preliminary analysis of the measurements made from the instrumented boreholes at AM01 and AM02 show the largest seasonal cycles in both potential temperature and salinity [*Rosenberg*, 2006]. Future analysis will focus on the synthesis of the instrumented borehole measurements and the connections of actual

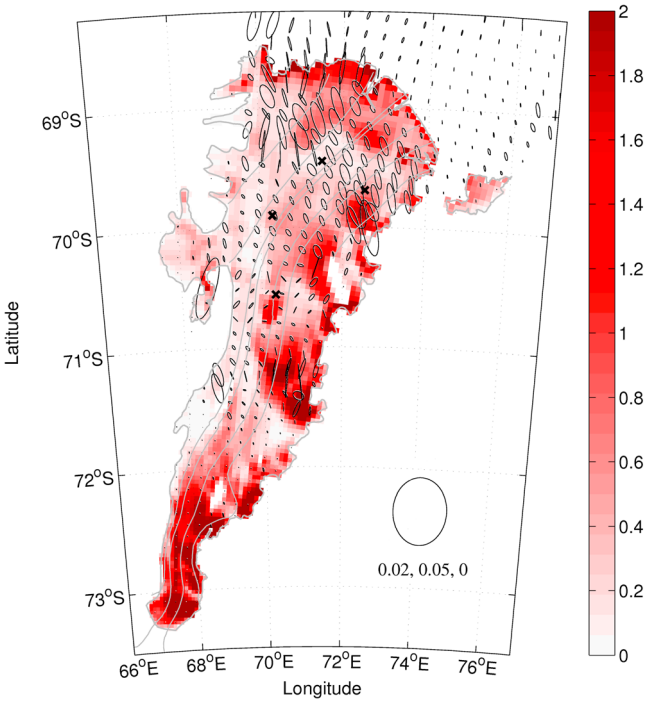

Figure 12. Melt/freeze standard deviation (m ice year^{-1}) over 3 years of simulation. The variance ellipses of the depth averaged velocity for every 3rd grid cell are also shown. The scale ellipse has a semi-major axis of 0.02 m^2 s^{-2}, a semi-minor axis of 0.05 m^2 s^{-2} and is orientated north.

oceanographic data and model output will be addressed elsewhere.

5. Conclusions

[54] We have presented results from a model of the AIS/Prydz Bay system. The main improvements of this model over previous studies are the inclusion of frazil dynamics and the use of the most up-to-date estimate of the sub ice shelf cavity geometry. The reference model performs well when compared to available oceanographic and glaciological estimates of the mass balance of the AIS. The model produces a net basal melt rate of 45.6 Gt year^{-1}. The melting at the base of the ice shelf seen in the model is primarily due to interaction with HSSW created from the surface sea-ice formation in winter. The ability to produce the water masses is influenced by spatially well-resolved open-ocean forcing fields and also implies that the surface forcing conditions are more important to consider than those for the lateral boundaries. Although the AIS is smaller than both the Ross Ice Shelf and Ronne-Filchner Ice Shelf, the amount of meltwater production is comparable. This is due to the larger thermal driving at the deep ice shelf regions (>2000 m) of the AIS, where the majority of the melt is thought to occur, compared to the shallower ice of the Ross and Filchner-Ronne ($\sim$1500 m). The temperature difference between the coldest open ocean water (at the surface freezing point) and the *in situ* freezing point of the deepest ocean water in contact with the AIS is $\sim$2 °C, leading to a melt rate that can exceed 30 m ice year^{-1}.

[55] The net accretion of marine ice is also in good agreement with independent glaciological estimates. Frazil initially forms in the supercooled water layer adjacent to the base of the ice shelf. The simulated accretion of marine ice is 5.26 Gt year^{-1}, which is comprised of 3.7 Gt year^{-1} of frazil accretion and only 1.6 Gt year^{-1} of direct basal refreezing. In the model without frazil the total accretion rate is 2.1 Gt, which is only due to direct basal refreezing. However, we find that, in the reference simulation, the accretion of frazil occurs earlier than is suggested by the observations. The simulations of frazil may be improved by using more frazil size classes. The present choice of 5 frazil size classes is due to the limitations of available computing power. Although there are no observations to confirm the actual distribution of frazil size beneath the AIS, the choice of 5 frazil classes yields model results in reasonable agreement with mass balance estimates. The parametrization of the frazil physics and marine ice accretion contains a large number of assumptions and represents one of the major sources of uncertainty in the model.

[56] Frazil growth moderates the maximum amount of supercooling found beneath the ice shelf. Importantly, the reduced level of supercooling manifests as enhanced basal refreezing through the precipitation of frazil. The frazil formation process leads to increased salinity and modifies both the horizontal and vertical circulation patterns of the sub-ice shelf cavity when compared to models without frazil. Here, we highlighted the importance of using a dynamic frazil model for marine ice accretion.

[57] However, a simpler approach for models that only aim to model deep water formation on climate time scales could be to simply remove excess bulk supercooling beneath the ice shelf, modifying both the temperature and salinity fields, and depositing the mass directly against the base of the ice shelf.

[58] The forcings applied to the model boundaries are about 10 years more recent than the observations made for the ice sheet mass balance. As our ocean boundary conditions are monthly averages over the observing time, which also show recent climate change, then they are likely to be biased towards a system that has already been affected by climate change when compared with pre-industrial forcing. However, the state of the ice shelf depends on the time scale of the response from any changes to the ocean. Two-way coupling to a larger global model would provide more realistic boundary conditions. A logical next step is to extend the present model to be forced with time series of forcing variables that overlap the satellite era.

[59] During the review of the glaciological mass balance estimates we identified a number of discrepancies between the most recent estimates of ice thickness that require further examination to improve mass balance estimates.

[60] Further simulations will involve determining the sensitivity of the ice shelf to a warming ocean and the application of the model to the cavities of other ice shelves.

Appendix A: Ice Shelf/Ocean Boundary

[61] The interface between the ice shelf and the ocean is parameterized using a viscous sub-layer, following [*Hellmer and Olbers*, 1989; *Scheduikat and Olbers*, 1990; *Hellmer et al.*, 1998; *Holland and Jenkins*, 1999]. This has been done previously for several simulations of the flow beneath ice shelves [e.g., *Beckmann et al.*, 1999; *Timmermann et al.*, 2002; *Holland et al.*, 2003]. Three equations represent the conservation of heat and salt and a linearized version of the equation of freezing point of seawater as a function of salinity and pressure. The free variables that are found by solving the three equations simultaneously are the temperature, T_b, and salinity, S_b, in the sub-layer at the ice shelf base, and the basal melt rate, m. The assumption is that the ice shelf is in a steady-state balance with respect to sources and sinks of mass and heat. The calculation of the actual heat and salt fluxes into the top model layer of the ocean includes the meltwater advection term that can be important in long simulations or with high basal melt rates [*Jenkins et al.*, 2001].

[62] The conservation of heat and salt, with the assumption that there is no salt present in the ice shelf, are:

$$\rho_i(L - c_i\Delta T)m = \rho c_w \gamma_T (T_b - T) \tag{A1a}$$

$$\rho_i S_b m = \rho \gamma_S (S_b - S) \tag{A1b}$$

where, ρ_i is the density of ice (assumed to be 916 kg m^{-3}), ρ is the density of ocean water, L is the latent heat of ice fusion (3.35×10^5), c_i and c_w are the specific heats of ice (2009 J kg^{-1} K^{-1}) and water (3974 J kg^{-1} K^{-1}), respectively. ΔT is the temperature difference between the ice shelf interior, T_i (-20°C), and the freezing temperature at the base of the ice shelf, T_f. T is the temperature and S the salinity of the water away from the base of the ice shelf base.

[63] The parameters γ_T and γ_S are coefficients that represent the transfer of heat and salt across the boundary layer.

Jenkins [1991] used a molecular sub-layer approximation to formulate expressions for γ_T and γ_S as:

$$\gamma_T = \frac{u_d}{2.12\ln(u_d h/\nu) + 12.5Pr^{2/3} - 9} \tag{A2a}$$

$$\gamma_S = \frac{u_d}{2.12\ln(u_d h/\nu) + 12.5Sc^{2/3} - 9} \tag{A2b}$$

where, the molecular Prandtl number (Pr) is the ratio of viscosity to thermal diffusivity and the molecular Schmidt number (Sc), is the ratio of viscosity to salinity diffusivity. The kinematic molecular viscosity of seawater, ν (1.95×10^{-6} m^2 s^{-1}), is considered constant [*Holland and Jenkins*, 1999] over the thickness of the boundary layer, h. The friction velocity, $u_d = \sqrt{c_d u^2}$, where c_d is a dimensionless drag coefficient (0.0025) and u is the velocity of the ocean. Note that the ice is considered to be stationary. The linearized version of the freezing point of seawater as a function of salinity and pressure is:

$$T_f = aS_b + b + cP \tag{A3}$$

where, T_f is the freezing point at the ice-ocean interface, a is the slope of liquidus for seawater (-5.73×10^{-2} °C psu^{-1}), b is the offset of liquidus for seawater (8.32×10^{-2} °C), c is the change in freezing temperature with pressure (-7.61×10^{-4} °C dbar^{-1}), and P is the pressure at the ice shelf base.

[64] Frazil laden water is considered to be a two-component mixture of ice and seawater that is treated as a homogeneous fluid with spatially-averaged properties. The total mass of frazil crystals within a fluid parcel is,

$$\mathrm{d}\mathcal{M}_\mathcal{C} = (\mathrm{d}\mathcal{M})\mathcal{C}, \tag{A4}$$

where $\mathrm{d}\mathcal{M} = \rho \mathrm{d}V$ is the total mass of the parcel of seawater (mass of water plus mass of frazil), and $\mathcal{C}$ is the mass fraction of frazil. For a unit volume of mixture the volume of the seawater fraction is $\rho(1-\mathcal{C})/\rho_s$ and the volume of the frazil fraction is $\rho\mathcal{C}/\rho_i$, where ρ_s is the density of the seawater without the ice fraction and $\rho\mathcal{C}$ is the mass of frazil per unit volume of seawater mixture. For a Boussinesq ocean model, the bulk density of the seawater is,

$$\rho = \rho_s + \rho\mathcal{C}\left(1 - \frac{\rho_s}{\rho_i}\right). \tag{A5}$$

[65] For Boussinesq fluid, the time tendency for frazil concentration takes the form,

$$\mathcal{C}_{,t} = -\nabla\cdot(\mathcal{C}\mathbf{v}) - \nabla\cdot(\mathbf{F}) + \mathcal{S} \tag{A6}$$

where the changes to the frazil mass can be mathematically represented by the convergence of tracer flux $\mathbf{F}$ and tracer source $\mathcal{S}$. For frazil that is suspended in the water column, $\mathbf{F}$ has properties that allow for (1) frazil buoyant rising and (2) the turbulent mixing of frazil crystals, which yields,

$$\underbrace{\frac{\partial\mathcal{C}}{\partial t}}_{\text{Transient}} + \underbrace{\nabla\cdot(\mathcal{C}\mathbf{v})}_{\text{Advection}} + \underbrace{w'\frac{\partial\mathcal{C}}{\partial z}}_{\text{Buoyant rising}} = \underbrace{\nabla\cdot(K\nabla\mathcal{C})}_{\text{Mixing}} + \underbrace{\mathcal{S}}_{\text{Source/Sink}} \tag{A7}$$

where w' is the buoyant rising velocity of frazil, z is the vertical coordinate (positive upwards), and K is the turbulent exchange coefficient (eddy diffusivity). The Regional Ocean Modeling System allows for the addition of extra tracers, with appropriate treatment of advection and diffusion of frazil.

[66] ROMS solves each term independently using a common numerical technique known as the "Method of Fractional steps" [*Yanenko*, 1971]. The terms in equation (A7) are solved in the sequence: buoyant rising, source/sink, horizontal advection, vertical advection, vertical diffusion, and finally horizontal diffusion.

[67] The source and sink terms for heat, salt and ice in the water are related to the melting and freezing of ice particles. Ice volume changes in the water are controlled by the flux of heat from crystals already present in the water column. The formulations of frazil boundary layers in the scientific literature make use of the assumption that the entire crystal is at the local freezing point: that is, there is a zero internal temperature gradient between the edge of the crystal in contact with the water and the center of the crystal. However, the analysis is complicated by the fact that the growth and melting of frazil is influenced by transfer of both heat and salt between the ocean and the surface of the ice crystals.

[68] The conservation equations for heat and salt due to frazil growth and melting are analogous to equations (A1a) and (A1b). With the assumption that heat diffusion into the crystals are negligible ($\Delta T = 0$) they can be written as:

$$\rho_i L f' = \rho c_w \gamma'_T \mathcal{A}(T_b - T) \tag{A8a}$$

$$\rho_i S_b f' = \rho \gamma'_S \mathcal{A}(S_b - S) \tag{A8b}$$

where, $\mathcal{A}$ is the surface area of frazil, f' is the rate of change of frazil volume and the coefficients for heat γ'_T and salt γ'_S are defined in terms of the Nusselt, Nu and Sherwood, Sh numbers, respectively,

$$\gamma'_T = \frac{\mathrm{Nu}k_T}{r} \tag{A9a}$$

$$\gamma'_S = \frac{\mathrm{Sh}k_S}{r} \tag{A9b}$$

where r is the radius of a disk shaped frazil crystal, $k_T = 1.4 \times 10^{-7}$ is the molecular thermal diffusivity of seawater and $k_S = 8 \times 10^{-10}$ is the molecular saline diffusivity. As with heat, the exchange of salt between the crystal surface and the ocean scales with the size of the crystal.

[69] The formulas for the exchange coefficients presented here are improved over those in previous literature [e.g., *Jenkins and Bombosch*, 1995]. Here, γ'_S is scaled by Sh (the mass transfer analogy of Nu), which is the ratio of turbulent mass transfer to mass diffusion. *Jenkins and Bombosch* [1995] scaled both γ'_T and γ'_S by Nu. Also, the exchange coefficients are scaled by the radius of the frazil disk, r [*Holland et al.*, 2007] and not the half-disk thickness, ra_r [*Jenkins and Bombosch*, 1995], where $a_r = 1/25$ is the disk aspect ratio. The effect of salt diffusion, as with that for heat, is strongly dependent on crystal radii.

[70] Utilizing the similarities in the equations between the ice growth rate at the base of an ice shelf and at the surface of an ice crystal, we can simplify the conservation equations

by omitting equation (A8b) and adding a scaling factor to equation (A8a). The scaling factor Θ in *Holland and Jenkins* [1999, equation (35)],

$$\Theta = 1 - \frac{aS_b c_w \gamma'_T}{L\gamma'_S} \tag{A10}$$

can be modified for frazil to include the formulations of γ'_T and γ'_S, presented here as,

$$\Theta' = 1 - \frac{aS_b c_w \mathrm{Nu} k_T}{L\mathrm{Sh} k_S}. \tag{A11}$$

[71] The scaling factor for heat transfer is important across all crystal radii and increases towards smaller frazil radii. Provided this factor is approximately constant, a two equation formulation with an effective transfer coefficient of γ'_T/Θ' should yield appropriate melt rates.

[72] In reality a spectrum of frazil crystals can exist within the plume at any one time. See *Daly* [1984] and *Morse and Richard* [2009] for more thorough reviews of the problem. The development of a multiple size class frazil model allows that the source of ice is adjusted for the volume concentration of the *i*-th class [*Smedsrud and Jenkins*, 2004; *Holland and Feltham*, 2005]. The frazil concentration $\mathcal{C}$ is distributed between N size classes such that:

$$\mathcal{C} = \sum_{i=1}^{N} \mathcal{C}_i. \tag{A12}$$

[73] Melting and freezing of frazil is modeled by the transfer of a certain number of frazil crystals from class n to the larger size class ($n + 1$) in the case of freezing, or smaller size class ($n - 1$) in the case of melting. Therefore, the rate change of frazil concentration in each class is determined by the difference in growth (melting) rates between class n and the class $n + 1$ ($n - 1$). Transfer processes between classes must also be consistent with the movement of the appropriate volume [*Smedsrud and Jenkins*, 2004].

[74] The melt/freeze of ice crystals is asymmetric: growth, G_i, occurs at the ice edges and melting, M_i, occurs over the entire crystal. This formulation assumes that the growth of frazil in turbulent seawater only occurs at the edge of the disk and melting occurs over the entire disk to give, assuming $T_f = T_b$:

$$G_i = \frac{c_w \mathrm{Nu}_i k_T}{L\Theta'_i}\left(T_f - T\right)\frac{2}{r_i^2}\mathcal{C}_i \tag{A13a}$$

$$M_i = \frac{c_w \mathrm{Nu}_i k_T}{L\Theta'_i}\left(T_f - T\right)\frac{2}{r_i}\left(\frac{1}{r_i} + \frac{1}{2a_r r_i}\right)\mathcal{C}_i. \tag{A13b}$$

[75] In these expressions Nu_i is Nu for each size class, i, which is calculated following *Holland et al.* [2007] and Θ'_i is calculated using equation (A11) for each size class. Note that, for $\Theta'_i = 1$, the expressions are those used in previous studies [*Smedsrud and Jenkins*, 2004; *Holland and Feltham*, 2005].

[76] The plume studies that have included frazil [e.g., *Holland and Feltham*, 2005; *Jenkins and Bombosch*, 1995] have all used strategies of introducing a small concentration of frazil crystals when the water becomes supercooled. Frazil seeding is due to dendrite-like platelet ice crystals growing on the ice shelf base that may be detached by eddies and suspended in the water column, providing frazil nuclei of various sizes. The seeding process used by these models makes no adjustment to the temperature and salinity when adding frazil seeds to the water column. In our model, if a cell becomes supercooled and does not contain frazil crystals, then the concentration of crystals in that cell is set to 1×10^{-7}, following the strategy of *Holland and Feltham* [2005]. Using a three-dimensional ocean model it is possible that supercooling can occur away from the surface boundary and, frazil nucleation sites are likely at all points in the water column. Seeding is thus allowed to occur at any cell in the model that becomes supercooled.

[77] Secondary nucleation is the process whereby frazil crystals of the largest size class can fragment into the smallest size class. The main processes thought to give rise to secondary nucleated seed crystals are collisions between frazil and detachment of surface irregularities by fluid shear [*Daly*, 1984]. The formulation used here follows that outlined in *Holland and Feltham* [2005] and allows for secondary nucleation process that include turbulent motions to create new seed crystals. The process is limited to produce a maximum number of seed crystals of 1×10^3 [*Smedsrud*, 2002].

[78] A frazil crystal in still water will rise at its terminal velocity when gravitational forces and drag forces are equal. The formulation choice for the rise velocity w' (mm/s) relative to the moving fluid is approximated using a recent empirical relationship between frazil size and rise velocity devised by *Morse and Richard* [2009] based on field observations of frazil formation in rivers. By fitting power laws to the data they developed a piecewise function:

$$w' = \begin{cases} 2.025D^{1.621} & \text{if } D \le 1.27\ \text{mm} \\ -0.103D^2 + 4.069D - 2.024 & \text{if } 1.27 < D \le 7\ \text{mm} \end{cases} \tag{A14}$$

where, $D = 2r$ is the diameter of a frazil crystal in mm.

[79] The precipitation of frazil onto the base of an ice shelf borrows from studies of sedimentation in the approach used by *Jenkins and Bombosch* [1995]. Each frazil size class, i will precipitate at a rate, p'_i:

$$p'_i = \frac{\rho_i}{\rho} w'_i \mathcal{C}\left(1 - \frac{|u|^2}{u_i^2}\right)\mathrm{He}\left(1 - \frac{|u|^2}{u_i^2}\right) \tag{A15}$$

where He is the Heaviside function, which prevents erosion from occurring, and u_i is a critical horizontal water velocity above which no precipitation can occur, and w'_i is the vertical rise velocity of the frazil crystal. This assumes that the flux of crystals that can precipitate out of the water column due to buoyancy is reduced by turbulence in the boundary layer adjacent to the ice shelf base. The critical velocity, u_i, is expressed as,

$$u_i^2 = \frac{0.05(\rho - \rho_i)g2r_i}{\rho c_d}. \tag{A16}$$

[80] Precipitation starts as soon as the velocity at the base of the ice shelf becomes lower than the critical velocity. The total precipitation rate, p', is

$$p' = \sum_{i=1}^{N} p'_i. \tag{A17}$$

Appendix B: Calculation of Variance Ellipses

[81] The velocity variance ellipses are calculated using the final 3 years output of 2.5 days resolution for the residual depth averaged velocities, $\overline{u'}$ and $\overline{v'}$. From these data the north/east velocity variance ($\overline{u'^2}$,$\overline{v'^2}$) and the covariance $\left(\overline{(u'v')^2}\right)$ are calculated. The magnitude and direction of the variability are represented using variance ellipses [see *Preisendorfer*, 1988]. The direction α of the axis of principal variability, measured anticlockwise from east is,

$$\tan\alpha = \frac{\sigma_{maj} - \overline{u'^2}}{\overline{(u'v')^2}} \tag{B1}$$

where the variance along the major axis, σ_{maj}, is

$$\sigma_{maj} = \frac{\overline{u'^2} + \overline{v'^2} + \sqrt{\left(\overline{u'^2 v'^2}\right)^2 + 4\left(\overline{(u'v')^2}\right)^2}}{2} \tag{B2}$$

and along the minor axis, $\sigma_{\min}$, is

$$\sigma_{\min} = \overline{u'^2} + \overline{v'^2} - \sigma_{maj} \tag{B3}$$

Anisotropic flow is represented by an elongated ellipse with the principal direction of the velocity variance aligned with the direction of the major axis. The orientation of the ellipse depends on the covariance $\left(\overline{(u'v')^2}\right)$; the major and minor ellipse axes define the coordinate system in which u' and v' are uncorrelated. Ellipses with a major axis orientated in the north-east/south-west are positively correlated and ellipses orientated to the north-west/south-east are negatively correlated [*Wilkin and Morrow*, 1994; *Morrow et al.*, 1994].

[82] **Acknowledgments.** Ben Galton-Fenzi was supported by the Australian Commonwealth Scientific and Industrial Research Organization and the University of Tasmania through the Quantitative Marine Science PhD program. This work was supported by the Australian Government's Cooperative Research Centres Program through the Antarctic Climate and Ecosystems Cooperative Research Centre (ACE CRC). Computing hours were provided by both the Tasmanian Partnership for Advanced Computing and the Australian National Computing Infrastructure under grant m68. The ROMS code was kindly provided by The ROMS/TOMS Group under the MIT/X License. Thanks to Paul Holland (British Antarctic Survey, U.K.) for allowing us to examine the frazil plume model code, Ian Allison (ACE CRC) for reading an early draft, Michael Dinniman (Old Dominion University, U.S.A.) for advice on using ROMS, and Michael Schodlok (NASA, JPL, U.S.A.) for advice on ECCO2. We also thank two anonymous reviewers.

References

Allison, I. (1979), The mass budget of the Lambert Glacier drainage basin, Antarctica, *J. Glaciol.*, *22*, 223–235.

Beckmann, A., H. H. Hellmer, and R. Timmermann (1999), A numerical model of the Weddell Sea: Large-scale circulation and water mass distribution, *J. Geophys. Res.*, *104*, 23,375–23,391.

Budd, W. F., M. J. Corry, and T. H. Jacka (1982), Results from the Amery Ice Shelf project, *Ann. Glaciol.*, *3*, 36–41.

Craven, M., I. Allison, H. Fricker, and R. Warner (2009), Properties of a marine ice layer under the Amery Ice Shelf, East Antarctica, *J. Glaciol.*, *55*(192), 717–728.

Daly, S. F. (1984), Frazil ice dynamics, *CRREL Monograph 84(1),* U.S. Army Corps of Eng., Cold Reg. Res. and Eng. Lab., Hanover, N. H.

Darelius, E., L. Smedsrud, S. Østerhus, A. Foldvik, and T. Gammelsrød (2009), Structure and variability of the Filchner Overflow Plume, *Tellus, Ser. A*, *61*(2), 446–464.

Determann, J. (1991), Numerical modelling of ice shelf dynamics, *Antarct. Sci.*, *3*(2), 187–195.

Determann, J., and R. Gerdes (1994), Melting and freezing beneath ice shelves: Implications from a three-dimensional ocean-circulation model, *Ann. Glaciol.*, *20*, 413–419.

Dinniman, M. S., J. M. Klinck, and W. O. Smith Jr. (2003), Cross-shelf exchange in a model of the Ross Sea circulation and biogeochemistry, *Deep Sea Res., Part II*, *50*, 3103–3120.

Dinniman, M. S., J. M. Klinck, and W. O. Smith Jr. (2007), Influence of sea ice cover and icebergs on circulation and water mass formation in a numerical circulation model of the Ross Sea, Antarctica, *J. Geophys. Res.*, *112*, C11013, doi:10.1029/2006JC004036.

Foldvik, A., T. Gammelsrød, E. Nygaard, and S. Østerhus (2001), Current measurements near Ronne Ice Shelf: Implications for circulation and melting, *J. Geophys. Res.*, *106*, 4463–4478, doi:10.1029/2000JC000217.

Fricker, H. A., G. Hyland, R. Coleman, and N. W. Young (2000), Digital elevation models for the Lambert Glacier-Amery Ice Shelf system, East Antarctica, from ERS-1 satellite radar altimetry, *J. Glaciol.*, *46*, 553–560.

Fricker, H. A., S. Popov, I. Allison, and N. Young (2001), Distribution of marine ice beneath the Amery Ice Shelf, *Geophys. Res. Lett.*, *28*(11), 2241–2244.

Fricker, H. A., N. W. Young, R. Coleman, J. N. Bassis, and J.-B. Minster (2005), Multi-year monitoring of rift propagation on the Amery Ice Shelf, East Antarctica, *Geophys. Res. Lett.*, *32*, L02502, doi:10.1029/2004GL021036.

Gade, H. G. (1979), Melting of ice in sea water: A primitive model with application to the Antarctic Ice Shelf and icebergs, *J. Phys. Oceanogr.*, *9*(1), 189–198.

Galton-Fenzi, B. K., C. Maraldi, R. Coleman, and J. Hunter (2008), The cavity under the Amery Ice Shelf, East Antarctica, *J. Glaciol.*, *54*(188), 881–887.

Galton-Fenzi, B. K., J. R. Hunter, R. Coleman, and N. W. Young (2012), A decade of change in the hydraulic connection between an Antarctic epishelf lake and the ocean, *J. Glaciol.*, *58*(208), 223–228, doi:10.3189/2012JoG10J206.

Gerdes, R., J. Determann, and K. Grosfeld (1999), Ocean circulation beneath Filchner-Ronne Ice Shelf from three-dimensional model results, *J. Geophys. Res.*, *104*(C7), 15,827–15,842.

Giovinetto, M. B., and H. J. Zwally (2000), Spatial distribution of net surface accumulation on the Antarctic ice sheet, *Ann. Glaciol.*, *31*, 171–178, doi:10.3189/172756400781820200.

Grosfeld, K., and H. Sandhager (2004), The evolution of a coupled ice shelf-ocean system under different climate states, *Global and Planet. Change*, *42*, 107–132.

Grosfeld, K., R. Gerdes, and J. Determann (1997), Thermohaline circulation and interaction between ice shelf cavities and the adjacent open ocean, *J. Geophys. Res.*, *102*(C7), 15,595–15,610.

Grosfeld, K., H. Sandager, and M. A. Lange (2001), Sensitivity of a coupled ice-shelf/ocean system to changed oceanographic boundary conditions, in *Forum for Research into Ice Shelf Processes (FRISP)*, *Tech. Rep. 14*, pp. 40–45, Bjerknes Centre for Climate Research, Bergen, Norway.

Hellmer, H. H. (2004), Impact of Antarctic ice shelf basal melting on sea ice and deep ocean properties, *Geophys. Res. Lett.*, *31*, L10307, doi:10.1029/2004GL019506.

Hellmer, H. H., and S. S. Jacobs (1992), Ocean interactions with the base of the Amery Ice Shelf, Antarctica, *J. Geophys. Res.*, *97*(C12), 20,305–20,317.

Hellmer, H. H., and D. Olbers (1989), A two-dimensional model for the thermohaline circulation under an ice shelf, *Antarct. Sci.*, *1*, 325–336.

Hellmer, H. H., S. S. Jacobs, and A. Jenkins (1998), Oceanic erosion of a floating Antarctic glacier in the Amundsen Sea, in *Ocean, Ice and Atmosphere Interactions at the Continental Margin*, *Antarct. Res. Ser.*, vol. 75, edited by S. S. Jacobs and R. F. Weiss, pp. 83–99, AGU, Washington, D. C.

Hemer, M. A., J. R. Hunter, and R. Coleman (2006), Barotropic tides beneath the Amery Ice Shelf, *J. Geophys. Res.*, *111*, C11008, doi:10.1029/2006JC003622.

Holland, D. M. (2001), An impact of sub-grid-scale ice-ocean dynamics on sea-ice cover, *J. Clim.*, *14*, 1585–1601.
Holland, D. M. (2002), Computing marine-ice thickness at an ice-shelf base, *J. Glaciol.*, *48*(160), 9–19.
Holland, D. M., and A. Jenkins (1999), Modeling thermodynamic ice-ocean interactions at the base of an ice shelf, *J. Phys. Oceanogr.*, *29*, 1787–1800.
Holland, P. R., and D. L. Feltham (2005), Frazil dynamics and precipitation in a water column with depth-dependent supercooling, *J. Fluid Mech.*, *530*, 101–124.
Holland, P. R., and D. L. Feltham (2006), The effects of rotation and ice shelf topography on frazil-laden ice shelf water plumes, *J. Phys. Oceanogr.*, *36*, 2312–2327.
Holland, D. M., S. S. Jacobs, and A. Jenkins (2003), Modelling the ocean circulation beneath the Ross Ice Shelf, *Antarct. Sci.*, *15*(1), 13–23.
Holland, P. R., D. L. Feltham, and S. Daly (2007), On the Nusselt number for frazil ice growth—A correction to "Frazil evolution in channels" by Lars Hhammar and Hung-Tao Shen, *J. Hydraul. Res.*, *45*(3), 421–424.
Holland, P. R., A. Jenkins, and D. M. Holland (2008), The response of ice shelf basal melting to variation in ocean temperature, *J. Clim.*, *21*, 2558–2572, doi:10.1175/2007JCLI1909.1.
Holland, P. R., H. F. J. Corr, D. G. Vaughan, A. Jenkins, and P. Skvarca (2009), Marine ice in Larsen Ice Shelf, *Geophys. Res. Lett.*, *36*, L11604, doi:10.1029/2009GL038162.
Jenkins, A. (1991), A one-dimensional model of ice shelf-ocean interaction, *J. Geophys. Res.*, *96*(C11), 20,671–20,677.
Jenkins, A., and A. Bombosch (1995), Modelling the effects of frazil ice crystals on the dynamics and thermodynamics of Ice Shelf Water plumes, *J. Geophys. Res.*, *100*(C4), 6,967–6,981.
Jenkins, A. and D. M. Holland (2002), A model study of ocean circulation beneath Filchner-Ronne Ice Shelf, Antarctica: Implications for bottom water formation, *Geophys. Res. Lett.*, *29*(8), 1193, doi:10.1029/2001GL014589.
Jenkins, A., H. H. Hellmer, and D. M. Holland (2001), The role of meltwater advection in the formulation of conservative boundary conditions at an ice-ocean interface, *J. Phys. Oceanogr.*, *31*, 285–296.
Jenkins, A., D. M. Holland, K. W. Nicholls, M. Schröder, and S. Østerhus (2004), Seasonal ventilation of the cavity beneath Filchner-Ronne Ice Shelf simulated with an isopycnic coordinate ocean model, *J. Geophys. Res.*, *109*, C01024, doi:10.1029/2001JC001086.
Kanamitsu, M., W. Ebisuzaki, J. Woollen, S. Yang, J. J. Hnilo, M. Fiorino, and G. L. Potter (2002), NCEP-DOE AMIP-II Reanalysis (R-2), *Bull. Am. Meteorol. Soc.*, *83*(11), 1631–1643.
King, M. A., R. Coleman, A.-J. Freemantle, H. A. Fricker, R. S. Hurd, B. Legrésy, L. Padman, and R. Warner (2009), A 4-decade record of elevation change of the Amery Ice Shelf, East Antarctica, *J. Geophys. Res.*, *114*, F01010, doi:10.1029/2008JF001094.
Kusahara, K., H. Hasumi, and T. Tamura (2010), Modeling sea ice production and dense shelf water formation in coastal polynyas around East Antarctica, *J. Geophys. Res.*, *115*, C10006, doi:10.1029/2010JC006133.
Large, W. G., J. C. McWilliams, and S. C. Doney (1994), Oceanic vertical mixing: A review and model with a nonlocal boundary layer parameterization, *Rev. Geophys.*, *32*, 363–403.
Lewis, E. L. (1985), The "Ice Pump", a mechanism for ice-shelf melting, in *Glaciers, Ice Sheets, and Sea Level: Effect of a CO_2-Induced Climate Change*, *Rep. DOE/EV/60235-1*, pp. 275–278, U.S. Dep. of Energy, Washington, D. C.
Losch, M. (2008), Modeling ice shelf cavities in a *z* coordinate ocean general circulation model, *J. Geophys. Res.*, *113*, C08043, doi:10.1029/2007JC004368.
MacAyeal, D. R. (1985), Evolution of tidally triggered meltwater plumes below ice shelves, in *Oceanology of the Antarctic Continental Shelves*, *Antarct. Res. Ser.*, vol. 43, pp. 109–132, AGU, Washington, D. C.
Maraldi, C., B. Galton-Fenzi, F. Lyard, L. Testut, and R. Coleman (2007), Barotropic tides of the southern Indian Ocean and the Amery Ice Shelf cavity, *Geophys. Res. Lett.*, *34*, L18602, doi:10.1029/2007GL030900.
Marsland, S. J., N. L. Bindoff, G. D. Williams, and W. F. Budd (2004), Modeling water mass formation in the Mertz Glacier Polynya and Adélie Depression, East Antarctica, *J. Geophys. Res.*, *109*, C11003, doi:10.1029/2004JC002441.
Martin, S., and P. Kauffman (1981), A field and laboratory study of wave damping by grease ice, *J. Glaciol.*, *27*, 283–313.
Meijers, A., A. Klocker, N. L. Bindoff, G. D. Williams, and S. J. Marsland (2010), The circulation and water masses of the Antarctic shelf and continental slope between 30 and 80°E, *Deep Sea Res., Part II*, *57*(9–10), 723–737, doi:10.1016/j.dsr2.2009.04.019.
Menemenlis, D., J.-M. Campin, P. Heimbach, C. Hill, T. Lee, A. Nguyen, M. Schodlock, and H. Zhang (2008), ECCO2: High resolution global ocean and sea ice data synthesis, *Mercator Ocean Q. Newsl.*, *31*, 13–21.
Morrow, R., R. Coleman, J. Church, and D. Chelton (1994), Surface eddy momentum flux and velocity variances in the Southern Ocean from Geosat altimetry, *J. Phys. Oceanogr.*, *24*, 2050–2071, doi:10.1175/1520-0485(1994)024.
Morse, B., and M. Richard (2009), A field study of suspended frazil ice particles, *Cold Reg. Sci. Technol.*, *55*, 86–102.
Mueller, R. D., L. Padman, M. S. Dinniman, S. Y. Erofeeva, H. A. Fricker, and M. A. King (2012), Impact of tide-topography interactions on basal melting of Larsen C Ice Shelf, Antarctica, *J. Geophys. Res.*, *117*, C05005, doi:10.1029/2011JC007263.
Murray, M. T. (1964), A general method for the analysis of hourly heights of the tide, *Int. Hydrogr. Rev.*, *41*(2), 91–101.
Nunes Vaz, R. A., and G. W. Lennon (1996), Physical oceanography of the Prydz Bay region of Antarctic waters, *Deep Sea Res., Part I*, *43*(5), 603–641.
Penrose, J. D., M. Conde, and T. J. Pauly (1994), Acoustic detection of ice crystals in Antarctic waters, *J. Geophys. Res.*, *99*(C6), 12,373–12,380.
Preisendorfer, R. W. (1988), *Principal Component Analysis in Meteorology and Oceanography*, 924 pp., Elsevier, Amsterdam.
Rignot, E. (2002), Mass balance of East-Antarctic glaciers and ice shelves from satellite data, *Ann. Glaciol.*, *34*, 217–227.
Rignot, E., and S. S. Jacobs (2002), Rapid bottom melting widespread near Antarctic ice sheet grounding lines, *Science*, *296*, 2020–2023.
Rosenberg, M. (2006), Amery Ice Shelf borehole microcat and CTD data, 2005/2006 season—Data processing and quality, *Tech. Rep. 15*, Antarct. Clim. and Ecosyst. Coop. Res. Cent., Hobart, Tas., Australia.
Scheduikat, M., and D. J. Olbers (1990), A one-dimensional mixed layer model beneath the Ross Ice Shelf with tidally induced vertical mixing, *Antarct. Sci.*, *2*(1), 29–42.
Shchepetkin, A. F., and J. C. McWilliams (2005), The regional oceanic modeling system (ROMS): A split-explicit, free-surface, topography-following-coordinate oceanic model, *Ocean Modell.*, *9*, 347–404.
Smedsrud, L. H. (2002), A model for entrainment of sediment into sea ice by aggregation between frazil-ice crystals and sediment grains, *J. Clim.*, *48*(160), 51–61.
Smedsrud, L. H., and A. Jenkins (2004), Frazil ice formation in an ice shelf water plume, *J. Geophys. Res.*, *109*, C03025, doi:10.1029/2003JC001851.
Stössel, A., M. M. Stössel, and J.-T. Kim (2007), High-resolution sea ice in long-term global ocean GCM integrations, *Ocean Modell.*, *16*, 206–223, doi:10.1016/j.ocemod.2006.10.001.
Tamura, T., K. I. Ohshima, and S. Nihashi (2008), Mapping of sea ice production for Antarctic coastal polynyas, *Geophys. Res. Lett.*, *35*, L07606, doi:10.1029/2007GL032903.
Timmermann, R., A. Beckmann, and H. H. Hellmer (2002), Simulations of ice-ocean dynamics in the Weddell Sea: 1. Model configuration and validation, *J. Geophys. Res.*, *107*(C3), 3024, doi:10.1029/2000JC000741.
Treverrow, A., R. Warner, W. Budd, and M. Craven (2010), Meteoric and marine ice crystal orientation fabrics from the Amery Ice Shelf, East Antarctica, *J. Glaciol.*, *56*(199), 877–890.
Vaughan, D. G., J. L. Bamber, M. Giovinetto, J. Russell, and A. P. R. Cooper (1999), Reassessment of net surface mass balance in Antarctica, *J. Clim.*,*12*, 933–946, doi:10.1175/1520-0442(1999)012.
Wen, J., K. C. Jezek, B. M. Csatho, U. C. Herzfeld, K. L. Farness, and P. Huybrechts (2007), Mass budgets of the Lambert, Mellor and Fisher Glaciers and basal fluxes beneath their flowbands on Amery Ice Shelf, *Sci. China D*, *50*(11), 1693–1706.
Wen, J., Y. Wang, J. Liu, K. C. Jezek, P. Huybrechts, B. M. Csatho, K. L. Farness, and B. Sun (2008), Mass budget of the grounded ice in the Lambert Glacier-Amery Ice Shelf system, *Ann. Glaciol.*, *48*, 193–197.
Wen, J., Y. Wang, W. Wang, K. C. Jezek, H. Liu, and I. Allison (2010), Basal melting and freezing under the Amery Ice Shelf, East Antarctica, *J. Glaciol.*, *56*, 81–90, doi:10.3189/002214310791190820.
Wilkin, J., and K. S. Hedström (1998), User's manual for an orthogonal curvilinear grid-generation package, report, 31 pp., Inst. of Mar. and Coastal Sci., Rutgers Univ., New Brunswick, N. J.
Wilkin, J. L., and R. A. Morrow (1994), Eddy kinetic energy and momentum flux in the Southern Ocean: Comparison of a global eddy-resolving model with altimeter, drifter, and current-meter data, *J. Geophys. Res.*, *99*, 7903–7916, doi:10.1029/93JC03505.
Williams, G. D., N. L. Bindoff, S. J. Marsland, and S. R. Rintoul (2008), Formation and export of dense shelf water from the Adélie Depression, East Antarctica, *J. Geophys. Res.*, *113*, C04039, doi:10.1029/2007JC004346.
Williams, M. J. M., K. Grosfeld, R. C. Warner, R. Gerdes, and J. Determann (2001), Ocean circulation and ice-ocean interaction beneath the Amery Ice Shelf, Antarctica, *J. Geophys. Res.*, *106*(C10), 22,383–22,399.
Williams, M. J. M., R. C. Warner, and W. F. Budd (2002), Sensitivity of the Amery Ice Shelf, Antarctica, to changes in the climate of the Southern Ocean, *J. Clim.*, *15*, 2740–2757.

Wong, A. P. S., N. L. Bindoff, and A. Forbes (1998), Ocean-ice interaction and possible bottom water formation in Prydz Bay, Antarctica, in *Ocean, Ice, and Atmospheres: Interactions at the Antarctic Continental Margin*, *Antarct. Res. Ser.*, vol. 75, edited by S. S. Jacobs and R. F. Weiss, pp. 173–187, AGU, Washington, D. C.

Wunsch, C., P. Heimbach, R. Ponte, I. Fukumori, and the ECCO-GODAE Consortium members (2009), The global general circulation of the ocean estimated by the ECCO Consortium, *Oceanography*, *22*(2), 88–103.

Yanenko, N. N. (1971), *The Method of Fractional Steps: The Solution of Problems of Mathematical Physics in Several Variables*, 160 pp., Springer, New York.

Young, N. W., and G. Hyland (2002), Velocity and strain rates derived from InSAR analysis over the Amery Ice Shelf, East Antarctica, *Ann. Glaciol.*, *34*, 228–234.

Yu, J., H. Liu, K. C. Jezek, R. C. Warner, and J. Wen (2010), Analysis of velocity field, mass balance, and basal melt of the Lambert Glacier–Amery Ice Shelf system by incorporating Radarsat SAR interferometry and ICESat laser altimetry measurements, *J. Geophys. Res.*, *115*, B11102, doi:10.1029/2010JB007456.